AGU ADVANCING EARTH AND SPACE SCIENCE

Earth and Space Science

RESEARCH ARTICLE
10.1029/2021EA001959

Rock Size-Frequency Distributions at the InSight Landing Site, Mars

M. P. Golombek[1], A. Trussell[1,2], N. Williams[1], C. Charalambous[3], H. Abarca[1], N. H. Warner[4], M. Deahn[4], M. Trautman[1], R. Crocco[1], J. A. Grant[5], E. Hauber[6], and R. Deen[1]

[1]Jet Propulsion Laboratory, California Institute of Technology, Pasadena, CA, USA, [2]California Institute of Technology, Pasadena, CA, USA, [3]Imperial College, London, UK, [4]SUNY Geneseo, Geneseo, NY, USA, [5]Center for Earth and Planetary Studies, National Air and Space Museum, Smithsonian Institution, 6th at Independence SW, Washington, DC, USA, [6]German Aerospace Center (DLR), Berlin, Germany

Key Points:

- Rocks measured within 10 m, 40 m, and ~500 m of the InSight lander cover 0.6–5%, ~3%, and 4–5% cumulative fractional area of the surface
- The rock size-frequency distributions observed from the orbit and the surface are on similar exponential model curves
- Rock abundance at InSight is between the Phoenix and Spirit landing sites and is consistent with orbital thermal imaging estimates

Correspondence to:
M. P. Golombek,
mgolombek@jpl.nasa.gov

Citation:
Golombek, M. P., Trussell, A., Williams, N., Charalambous, C., Abarca, H., Warner, N. H., et al. (2021). Rock size-frequency distributions at the InSight landing site, Mars. *Earth and Space Science*, *8*, e2021EA001959. https://doi.org/10.1029/2021EA001959

Received 10 AUG 2021
Accepted 10 NOV 2021

Author Contributions:
Conceptualization: M. P. Golombek
Data curation: N. Williams
Formal analysis: M. P. Golombek, A. Trussell, N. Williams, C. Charalambous, M. Deahn, M. Trautman, R. Crocco
Investigation: M. P. Golombek, N. H. Warner, M. Deahn
Methodology: A. Trussell, N. Williams, C. Charalambous, H. Abarca, N. H. Warner, M. Deahn, M. Trautman, R. Crocco, R. Deen
Software: N. Williams, M. Trautman, R. Crocco, R. Deen
Validation: H. Abarca

Abstract Rocks around the InSight lander were measured in lander orthoimages of the near field (<10 m), in panoramas of the far field (<40 m), and in a high-resolution orbital image around the lander (1 km^2). The cumulative fractional area versus diameter size-frequency distributions for four areas in the near field fall on exponential model curves used for estimating hazards for landing spacecraft. The rock abundance varies in the near field from 0.6% for the sand and pebble-rich area to the east within *Homestead hollow* to ~3–5% for the progressively rockier areas to the south, north, and west. The rock abundance of the entire near field is just over 3%, which falls between that at the Phoenix (2%) and Spirit (5%) landing sites. Rocks in the far field (<40 m) that could be identified in both the surface panorama and a high-resolution orbital image fall on the same exponential model curve as the average near-field rocks. Rocks measured in a high-resolution orbital image (27.5 cm/pixel) within ~500 m of the lander that includes several rocky ejecta craters fall on 4–5% exponential model curves, similar to the northern and western near-field areas. As a result, the rock abundances observed from orbit fall on the same exponential model rock abundance curves as those viewed from the surface. These rock abundance measurements around the lander are consistent with thermal imaging estimates over larger pixel areas as well as expectations from fragmentation theory of an impacted Amazonian/Hesperian lava flow.

1. Introduction

The size-frequency distribution (SFD) of rocks on Mars is important for understanding the geologic and geomorphic history of the surface (e.g., Garvin et al., 1981; Ward et al., 2005; Yingst et al., 2007, 2010, 2013, 2016; Grant et al., 2006; Craddock & Golombek, 2016), for determining the aerodynamic roughness important for eolian processes (Hébrard et al., 2012; Charalambous et al., 2020), for quantifying the hazards for landing spacecraft (Golombek and Rapp, 1997; Golombek, Haldemann et al., 2003; Golombek et al., 2008; Golombek, Huertas et al., 2012; Mastropietro et al., 2020), and for evaluating the trafficability for roving (Golombek, Grant et al., 2012; Golombek, Otero et al., 2017; Pajola et al., 2017). In this regard, rocks are defined as naturally occurring solid masses on the surface that are distinct from finer grained soils and would include boulders, cobbles, and pebbles in traditional particle/grain-size scales. Rock counts have been made by all the landers or rovers on the surface of Mars and they have been related to various functions to fit their size-frequency distributions (SFD). Initially, power law distributions were used to fit measured Viking lander rock distributions (Binder et al., 1977; Moore et al., 1979), and single fragmentation events are expected to be fractal and scale invariant and so can be represented by a power law (Turcotte, 1997). Although power laws do reasonably fit portions of rock size-frequency distributions, which show up as straight lines when plotted on log-log plots of the cumulative number of rocks (normalized by area) versus rock diameter (e.g., Hartmann, 1969), they invariably overestimate the number (or area) covered by large and small rocks. In addition, power laws must have defined size ranges over which they are valid. Exponential models of the cumulative fractional area versus diameter of rocks at the Mars landing sites avoid the overestimation of large rocks and small particles (Golombek & Rapp, 1997) and are generally similar to Rosin Rammler and Weibull distributions that have also been used previously to describe rock populations (Rosin & Rammler, 1933; Gilvarry, 1961; Gilvarry & Bergstrom, 1961; Schröder et al., 2021), which predict that ubiquitous flaws or joints will lead to exponentially fewer blocks with increasing size during weathering and transport (e.g., Wohletz et al., 1989; Brown, 1989; Brown & Wohletz, 1995).

Writing – original draft: M. P. Golombek, C. Charalambous, M. Deahn, M. Trautman
Writing – review & editing: N. Williams, N. H. Warner, J. A. Grant, E. Hauber

The advent of High-Resolution Imaging Science Experiment (HiRISE) images at ~30 cm/pixel showed that the SFD of rocks >1.5 m diameter measured from orbit and smaller rocks from the surfaces of landing sites fall on the same exponential model curve (Golombek et al., 2008, Golombek, Kass et al., 2020). These observations support the use of HiRISE images to measure rocks >1.5 m diameter, fitting these rocks to an exponential SFD model and extrapolating along the model to predict the number of rocks smaller than 1.5 m that could be potentially hazardous to landing spacecraft (Golombek et al., 2008; Golombek, Grant et al., 2012; Golombek, Huertas et al., 2012; Golombek, Kipp et al., 2017; Golombek, Otero et al., 2017). These fits also show that the lognormal models for the rock size-frequency distributions on Mars proposed by Hébrard et al. (2012) to derive an aerodynamic roughness map for atmospheric and eolian studies severely underestimate the number or area covered by large rocks (Golombek, Huertas et al., 2012). The exponential model equations are of the form: $F_k(D) = k\ exp\ [-q(k)\ D]$, where $F_k\ (D)$ is the cumulative fractional area (CFA) covered by rocks of diameter D or larger, k is the fraction of the total area covered by all rocks, and an exponential $q(k)$ that governs how abruptly the fraction of the total area covered by rocks decreases with increasing diameter (Golombek & Rapp 1997), which is approximated by $q(k) = 1.79 + 0.152/k$. These distributions form a family of non-crossing curves that flatten out at small rock diameters. Note that these models are based on the area covered by rocks (diameter squared), which when translated into cumulative number per m^2 distributions by numerical integration on a log-log plot result in a less curved distribution than a true exponential (e.g., Golombek, Haldemann et al., 2003, 2008, Golombek, Huertas et al., 2012; Craddock & Golombek, 2016) that can be fit more readily to power law distributions over a limited diameter range (e.g., Grant et al., 2006; Russell et al., 2013).

Charalambous (2014) has shown that repeated fragmentation events, each of which is scale invariant (fractal) or a power law (Turcotte, 1997), result in a particle size-frequency distribution described by a negative binomial (NB) function that resembles the exponential models (and similar Weibull distributions). Rock counts in nearly complete HiRISE coverage of the InSight landing site were fit by a NB function and predicted by the observed cratering (Golombek, Kipp et al., 2017) and resulted in simulated surface and subsurface rock distributions that are consistent with observations at the surface (Charalambous et al., 2019; Golombek, Kass et al., 2020). Finally, a composite size-frequency distribution of particles (rocks to dust) can be explained by fragmentation due to impact for particles above 0.2–0.5 mm, with eolian activity responsible for the reduction below this size; together these processes can produce the global surface layer of mostly sand-sized particles on Mars (Golombek, Charalambous et al., 2018, 2020).

The NASA InSight mission (Interior Exploration using Seismic Investigations, Geodesy, and Heat Transport) landed in November 2018 and has acquired a number of panoramas (Golombek, Warner et al., 2020) using an arm-mounted color camera (Instrument Deployment Camera, IDC, Maki et al., 2018) with stereo images that have been made into a nearly complete digital elevation model (DEM) and orthomosaic (used to measure features such as rocks). InSight landed in western Elysium Planitia within a quasi-circular depression, interpreted to be ~27 m diameter, degraded impact crater (Warner et al., 2020), informally named *Homestead hollow*, with a smooth pebble-rich surface adjacent to a slightly rockier and rougher terrain, referred to as Rocky field (Golombek, Warner et al., 2020). The broader surface appears modified by impact, eolian, and lesser mass wasting processes with craters in various stages of degradation (Golombek, Warner et al., 2020).

Prior to landing, orbital estimates of rock abundance in the landing ellipse indicated a surface with very low average rock abundance (Golombek, Kipp et al., 2017). In HiRISE measurements of >50 images, the average cumulative fractional area (CFA) covered by rocks is ~1–2% away from craters with obvious rocks in their ejecta (so-called rocky ejecta craters). Using all rocks within the ellipse, including sparse rocky ejecta craters, yields a CFA of ~6%. These low rock abundances are consistent with thermal imaging estimates of rock abundance (<5%) (Christensen, 1986; Nowicki and Christensen, 2007) and are generally comparable with rock distributions measured at the Phoenix and Spirit landing sites (Golombek, Kipp et al., 2017).

After landing, initial rock counts were performed in a number of small (1–7 m^2) areas around the lander that had stereo coverage (Golombek, Warner et al., 2020, Golombek, Kass et al., 2020). These counts showed surfaces with rock abundance of 1–4% that were generally similar to and bounded by the rock abundances at the Phoenix and Spirit landing sites. This paper presents the rock counts and SFD in the nearly complete DEM panorama, which covers more area (~200 m^2) and is a better representation of the rock population around the lander. We also measured rocks that can be identified in both a HiRISE image and surface panorama in the far field, extending out to ~40 m from the lander. In addition, the largest individual rocks as well as distributions around the lander are

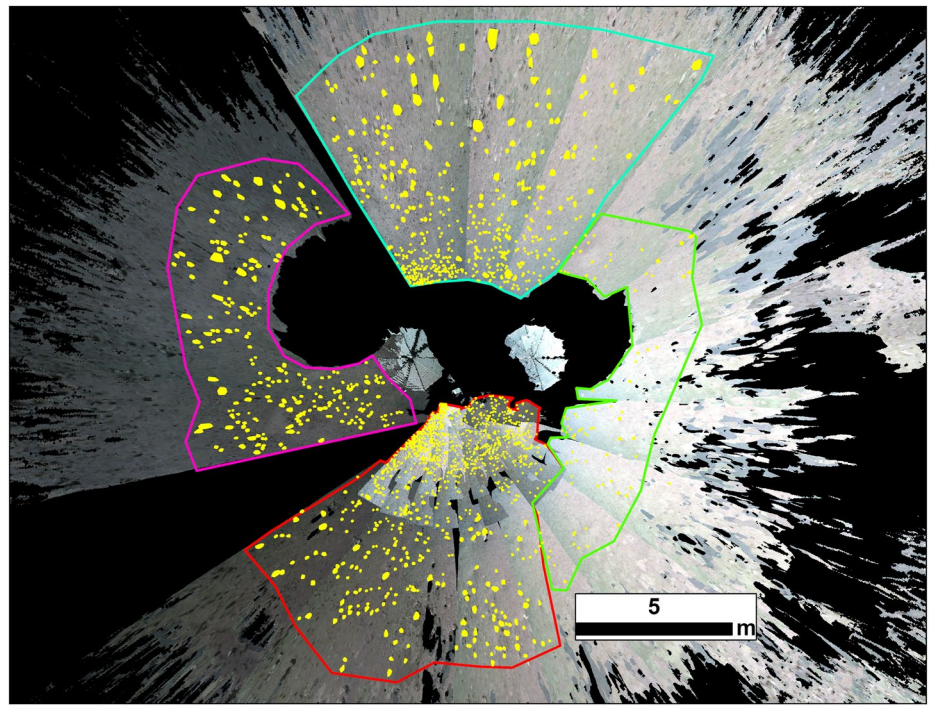

Figure 1. Orthomosiac (north up), produced from panorama digital elevation model, of the four areas around the InSight lander in which rocks (yellow) were counted (North, dark green; South, red; East, light green; West, pink). The N area is largest and the E area is the smallest. The S area has the largest number of rocks. Note the breaks in the extent of the areas produced by the occlusions from the solar panels to the east and west, the limited stereo coverage downslope to the east, and gaps separating the west area from the rest of the orthomosaic.

compared to rocks measured in the area around the lander in HiRISE. Results indicate that the >1.5-m diameter rocks measured in HiRISE images fall on the same exponential model curves as those measured on the ground and that the SFD is well represented by exponential model curves for CFAs of 1–5%. We begin with rocks measured around the lander in the panorama orthoimage and discuss their SFD. Next, we measure rocks in the far field that can be seen in InSight and HiRISE images, derive their SFD, and compare the largest ones to those measured in HiRISE. We present the HiRISE rock SFD in a km-size area around the lander and compare the results from those acquired from the lander and discuss their implications for Mars rock SFDs and fragmentation theory.

2. Near-Field Rock Distributions

2.1. Panorama DEM and Orthomosaic

IDC stereo images (N = 283) acquired on Sols 12–160 were mosaicked to create a panorama DEM and the orthoimage shown in Figure 1. The images for the DEM were acquired in 5 sections with vertical and horizontal stereo offsets to fill in the 360° as well as the upper right quadrant of all images where the arm obstructs the terrain. Image scale varied from 0.12 cm/pixel to 2.8 cm/pixel with increasing distance and the DEM has elevation postings every 5 mm. The panorama orthomosaic has been bundle adjusted (Abarca et al., 2019), except for the west region, which does not overlap with the rest of the panorama. Stereo coordinates have multiple sources of error stemming from the robotic arm position uncertainty and stereo processing errors (from stereo range and camera model errors). During pre-launch testing, error analysis and stereo processing were focused on the workspace region in front of the lander where the instruments were to be deployed by the robotic arm. Tests showed that the workspace DEM had a mean horizontal accuracy of 11 mm, a mean absolute vertical accuracy of 6.5 mm, and a mean relative vertical accuracy of 5 mm. After landing, the sol 12 workspace images (N = 56) in front of the lander had a spatial accuracy between adjacent stereo frames of 1.9 mm overall with a maximum error between frames of 4 mm. Images beyond the workspace, including horizon images, were bundle adjusted to those in the workspace. Arm uncertainty increases when the robotic arm is positioned to image the horizon due to the motions

Table 1
Area and Number of Rocks and Those >3 cm Diameter Counted in Four Near-Field Regions Around InSight

Region	Area (m^2)	All rocks	Rocks >3 cm
North	75.29	533	328
East	30.69	90	45
South	60.13	1160	266
West	41.20	234	215
All	207.31	2017	854

that are required to reach these imaging poses. The arm uncertainty and minimal overlap between frames led to large vertical seams 10 cm wide between the 3 sections of the panorama DEM and up to 25 cm behind the lander. The error within each stereo pair, however, is characterized by the stereo range error (Maki et al., 2018) of the IDC camera. Range error in the DEM spans from 9 mm closest to the rover in the workspace to roughly 13 cm at the 10 m range. The position of the IDC images when they were acquired was in the IDA (Instrument Deployment Arm) robotic arm frame and were translated to the Site Frame (positive north and east coordinates), which corrects for spacecraft tilt and orientation provided by the inertial measurement unit (IMU). Comparison of azimuths to features identified in both the surface, controlled panorama and a hierarchically georeferenced HiRISE orthoimage of the landing site shows azimuths agree to <1°, which is the expected accuracy of the IMU (Golombek, Williams et al., 2020).

2.2. Method

The orthomosiac and DEM were divided into four subareas in the north, south, east, and west directions based on contiguous areas with similar coverage and breaks between them produced by occlusions of the surface from the solar panels to the east and west, the limited stereo coverage downslope to the east (Golombek, Williams et al., 2020), and gaps in the orthomosaic to the northwest and southwest (Figure 1, Table 1). These areas correspond to mapped morphologic surface units with the smooth terrain filling the degraded impact crater *Homestead hollow* to the east, rougher and rockier terrain of Rocky field (impact ejecta) to the north and west, and the transition between them to the south (Golombek, Warner et al., 2020; Grant et al., 2020). Rocks larger than 0.01 m were measured by digitizing polygonal outlines of visible rocks in the orthomosiac in ArcGIS Pro (Figure 2). A convex hull, which is the smallest convex polygon enclosing the rock (representing the minimum bounding geometry), was calculated providing minimum and maximum (non-vertical) axes. The minimum axis is calculated as the shortest distance between any 2 vertices of the minimum bounding polygon, while the maximum axis is calculated as the longest distance between any 2 vertices of the minimum bounding polygon. Measurements in the orthomosaic are exactly horizontal with no elevation information. These two axes were averaged to yield an average rock diameter in meters as is standard practice for plotting rock size-frequency distributions. The area of each quadrant was calculated by drawing a polygonal shape around the edges of each visible mapping space, which excluded gaps in the orthomosaic (Table 1). Size-frequency distributions were then calculated for each region over its given area. All measurements and areas were then combined to give a size-frequency distribution for all rocks in the orthomosaic. The four areas measured range from 31 m^2 to 75 m^2 and included 90–1160 rocks

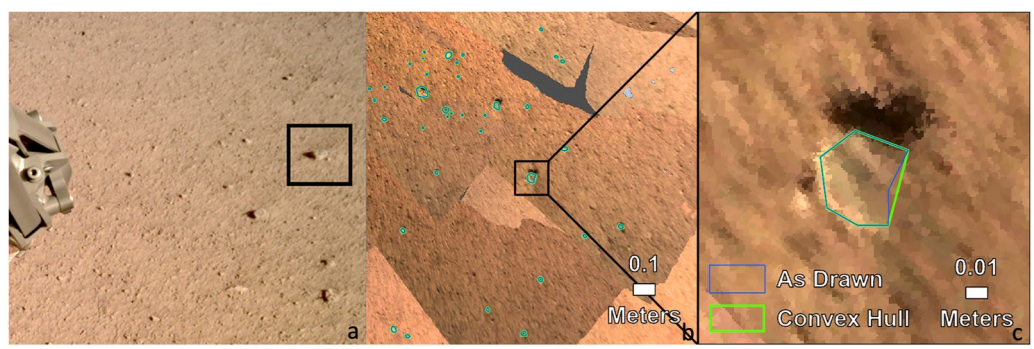

Figure 2. Rock measurement method using a convex hull. (a) IDC surface image of a portion of the workspace to the southeast showing small pebbles and example (black box) measured. (b) Portion of the orthomosaic showing the same pebble that is expanded in (c). (c) Digitized polygonal outline of the pebble in blue and the convex hull calculated in ArcGIS in green (note slight difference), which is the smallest convex polygon enclosing the rock representing the minimum bounding geometry, from which the minimum and maximum axes were determined. Panel (a) is IDC image D050R0012_597606285EDR_F0101_0060M3. Note that orthomosaics in (b) and (c) are rotated about 140° clockwise with respect to panel (a).

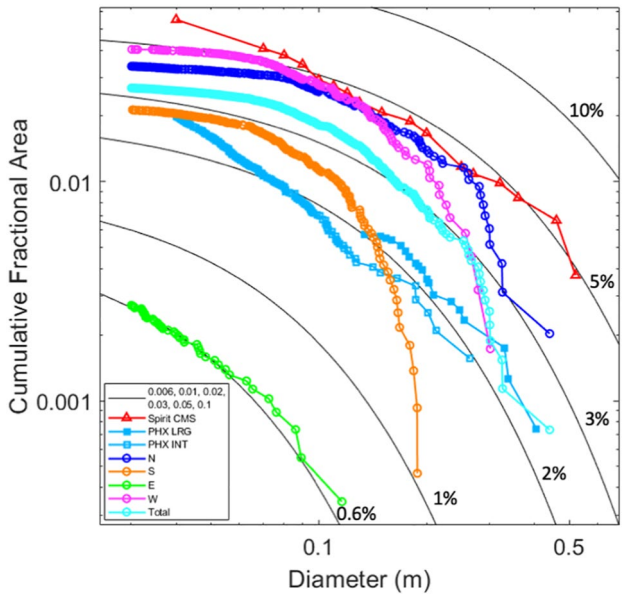

Figure 3. The cumulative fractional area of rocks larger than any given diameter versus diameter of the rocks measured in the four near-field areas: north (N), south (S), east (E), and west (W) shown in Figure 1, and all near-field rocks along with exponential model curves (black) for different total CFA (annotated) or k of 0.6%, 1%, 2%, 3%, 5%, and 10% (Golombek & Rapp, 1997). Also shown are the rocks measured at the Phoenix (Heet et al., 2009; Golombek, Huertas et al., 2012) and Spirit landing sites (Golombek et al., 2006) as plotted in Golombek, Huertas et al. (2012).

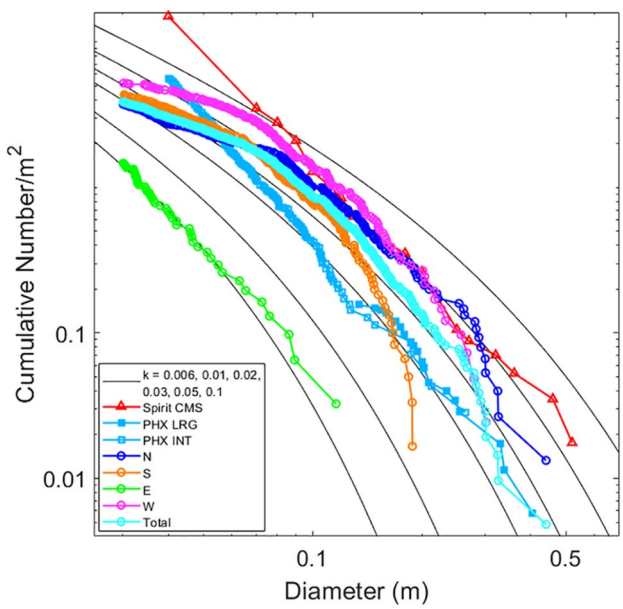

Figure 4. The cumulative number of rocks per m^2 larger than any given diameter versus diameter of the rocks measured in the four near-field areas: north (N), south (S), east (E), and west (W) shown in Figure 1 and all near-field rocks along with equivalent exponential model curves for different total CFA or k shown (Golombek & Rapp, 1997; Golombek, Haldemann et al., 2003). Also shown are the rocks measured at the Phoenix (Heet et al., 2009; Golombek, Huertas et al., 2012) and Spirit landing sites (Golombek et al., 2006) as plotted in Golombek, Huertas et al. (2012).

and extend from the center of the lander ~4–6 m to the east to ~1–10 m to the south. The total area is 207.3 m^2 and the total number of rocks counted is 2017; the total number of rocks >3 cm diameter is 854. The size-frequency distributions are reported for rocks >3 cm diameter and are shown on log-log plots. Although spatial uncertainties in the orthomosaic of <4 mm in the workspace to <1 cm at 10 m distance are estimated, uncertainties in the measurements of rocks over small distances within the orthomosaic are much less and do not have an appreciable effect on the rock measurements.

2.3. Size-Frequency Distributions

The near-field size-frequency distribution of CFA versus diameter or rock abundance around the InSight lander varies from <1% to ~5% (Figure 3). The least rocky, smooth plain surface of *Homestead hollow* to the east of the lander, falls on a model SFD curve for 0.6% CFA. The SFD of the highest rock abundance area to the west of the lander in the rougher and rockier terrain of Rocky field falls on a model 5% CFA for diameters <10 cm, but drops to between the 2–3% model curves for the largest diameters. The SFD of the area to the north, which is also in Rocky field, includes the largest rock counted (44 cm) and rises from ~3% model CFA for the largest rocks to ~4.5% for diameters <30 cm. The area to the south of the lander, which is the transition between the smooth and rocky terrains, rises from ~1% model CFA at 20 cm diameter to just below 3% model CFA for diameters <10 cm. The SFDs of all areas are generally parallel to the exponential model curves at diameters <10–30 cm. All areas, except the area to the east, fall below the models for larger diameters, indicating a relative deficiency of large rocks. The entire area together has a SFD that is close to the exponential 3% model curve for diameters 15–30 cm and a 3.4% model curve for rocks smaller than 12 cm.

These SFDs are generally similar to initial counts obtained over smaller areas (Golombek, Warner et al., 2020; Golombek, Williams et al., 2020), except the range in rock abundance is greater and the SFDs are clearly curved on the log-log plot and more closely resemble the curved exponential model SFDs than the initial smaller area counts, some of which approximate power laws (straight lines). *Homestead hollow* has the lowest rock abundance (0.6%) and the area to the north and west has the highest (4–5%). The lower rock abundance within the hollow likely reflects a real paucity of rocks within the fill as compared to exterior surfaces due to more significant burial by infilling sediments (Grant et al., 2020). The average rock abundance for the entire area counted is ~3%, which is between ~2% at the Phoenix and 5% at the Spirit landing sites. The rockier areas to the north and west (4–5%) are more representative of the area around the lander that includes rocky ejecta craters (Golombek, Kass et al., 2020), compared with the rock-poor area of *Homestead hollow*. The rockier area to the west is probably from rays of ejecta from younger nearby craters (Grant et al., 2020).

The cumulative number of rocks (per m^2) larger than any given diameter versus diameter plot for the four areas and total SFD indicate generally similar total rock abundances with some subtle differences (Figure 4). The model curves in this plot are less curved than in CFA plots, because they are numerically integrated from the exponential CFA models where the area is the diameter squared versus the cumulative number (diameter not squared). The cumulative number SFD of the area to the east of the lander in *Homestead hollow* also falls on the 0.6% model curve. The SFD of the area to the west of the lander rises from the 3% model curve for a rock diameter of 0.3 m

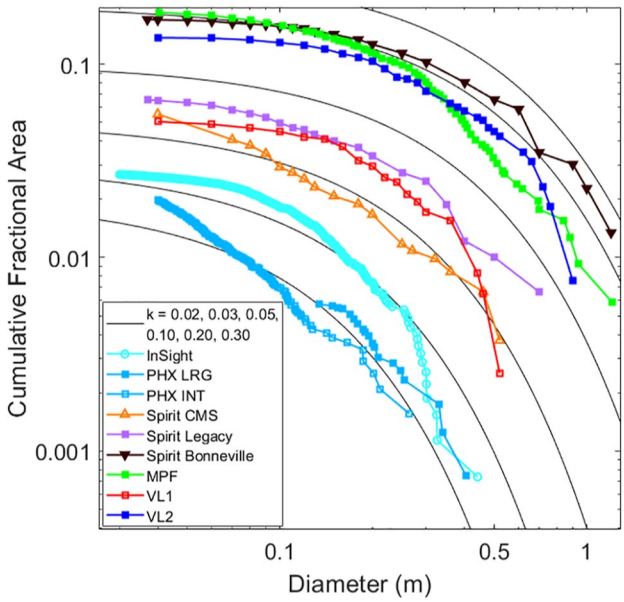

Figure 5. The cumulative fractional area of rocks larger than any given diameter versus diameter of the rocks measured from the surface of Mars along with exponential model curves for different total CFA or k of 2%, 3%, 5%, 10%, 20%, and 30% (Golombek & Rapp, 1997). Sources of rocks measured at Viking Lander 1, Viking Lander 2 (Moore & Keller, 1990, 1991), Mars Pathfinder (Golombek, Haldemann et al., 2003), Spirit (Golombek et al., 2006), Phoenix (Heet et al., 2009; Golombek, Huertas et al., 2012) (all replotted in Golombek, Huertas et al., 2012), and InSight (this paper).

to about 5% for a rock diameter of <0.2 m. At diameters below 0.2 m, the west SFD is between the 5% and 10% model curves before decreasing to ~3% at 0.03 m. The shape of the SFDs for the areas to the south, north, and total is similarly more curved than the model distributions (and clearly not straight lines expected for power law distributions) with fewer rocks at large and small diameters compared with intermediate diameters. In addition, the intermediate cumulative number of SFDs for the areas to the south and north is parallel to model curves with slightly higher CFA than the CFA SFD plots in Figure 3 (the area to the south is ~5% and the area to the north is ~6%).

The exponential CFA model SFDs were developed for hazard analysis of landing spacecraft on Mars in which large rocks that can damage spacecraft are important. For Mars Pathfinder, Mars Exploration Rover, Mars Science Laboratory, and the Mars 2020 Rover, rocks of concern are about 0.5 m high or ~1 m diameter for hemispherical rocks (Golombek et al., 1997, Golombek, Grant et al., 2006, 2012) and 0.35–0.45 m height or ~0.7–0.9 m diameter for Phoenix and InSight (Arvidson et al., 2008; Golombek, Kipp et al., 2017). Rock SFDs at most of the landing sites reasonably follow the exponential curves down to around 0.03 m diameter (Figures 5 and 6). However, for SFDs at the Phoenix and Spirit landing sites, rocks with diameters <0.06 m, have slopes that are steeper than the model SFDs and appear more power law like (straight line on these log-log plot) (Figures 5 and 6). For the plots of InSight rocks, we cut the SFDs off at 0.03 m diameter, but rocks with smaller diameter were measured (Table 1). Rocks smaller than 0.03–0.08 m diameter become progressively more difficult to map farther from the lander as the resolution decreases and small rocks are occluded by larger rocks. To assess this effect, we created CFA and cumulative number SFD plots of incremental 1-m wide annuli with increasing distance from the lander. Although comparison of the SFD for annuli close to the lander did flatten at smaller diameter than those farther away, all did flatten by 0.01-0.03 m diameter, except the area to the south. The area to the south is closest to the lander (and arm), with the highest resolution images, and has no large rocks (>0.12 m) (Figures 1–3), and the SFD does appear power law like for diameters <0.05 m. Nevertheless, all areas combined together do not show this behavior, so the InSight lander rock SFD does not have a steeper slope than the models such as the Phoenix and Spirit landing sites. We attribute the power law behavior of the SFD of the workspace counts reported in Golombek, Warner et al. (2020) and Golombek, Williams et al. (2020) to be due to the small areas counted and the limited diameter range (i.e., the lack of large rocks).

The rock SFD of the InSight landing site are generally similar in shape to local rock measurements made at other landing sites on Mars. The shape of the SFD of CFA versus diameter plot of the InSight landing site is generally similar to the other landing sites and the exponential model distributions (Figure 5). Furthermore, the deficit of large rocks counted compared to the models at the InSight landing site is also observed for the Viking Lander 1, Viking Lander 2, and Mars Pathfinder sites even though these sites have higher rock abundances of around 7%, 16%, and 19%, respectively (Figure 5). Comparison with the SFD of rocks in HiRISE images for these sites indicates that this deficit does not extend to larger diameter (Golombek et al., 2008; Golombek, Huertas et al., 2012), indicating that the effect is due to the generally small areas measured around the landers and the statistics of including larger rocks in these small areas. The InSight landing site rock abundance of ~3% is greater than the Phoenix landing site (~2%) and less than the Spirit landing site (5%), Viking Lander 1 (~7%), the Spirit Legacy site (7%), and the Spirit Bonneville site (~20%).

The SFD of the cumulative number per m^2 versus the diameter plot of the InSight landing site is also similar in shape to local rock measurements at other landing sites on Mars (Figure 6). In particular, the shape of the rock cumulative number SFDs for InSight is similarly more curved than the model distributions with fewer rocks at large and small diameters compared with intermediate diameters such as the SFDs at Viking Lander 1, Viking Lander 2, and Mars Pathfinder even though these sites have higher CFAs. None of these are straight lines as expected for power law distributions. In addition, the cumulative number SFD for InSight is parallel to model curves with

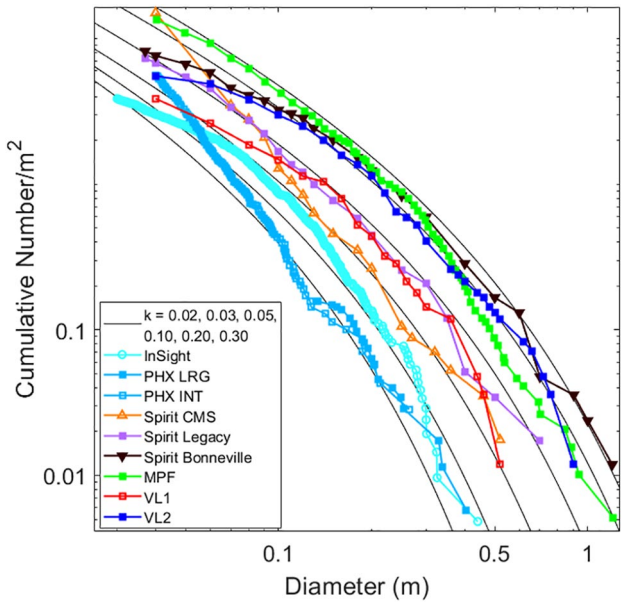

Figure 6. The cumulative number of rocks per m^2 larger than any given diameter versus diameter of the rocks measured from the surface of Mars along with equivalent exponential model curves for different total CFA or k shown (Golombek & Rapp, 1997; Golombek, Haldemann et al., 2003). Sources of rocks measured at Viking Lander 1, Viking Lander 2 (Moore & Keller, 1990, 1991), Mars Pathfinder (Golombek, Haldemann et al., 2003), Spirit (Golombek et al., 2006), Phoenix (Heet et al., 2009; Golombek, Huertas et al., 2012) (all replotted in Golombek, Huertas et al., 2012), and InSight (this paper).

higher CFA at intermediate diameters than the CFA SFD (~5%), similar to the intermediate diameter SFDs at Viking Lander 1 (~10%), Viking Lander 2 (20%), Mars Pathfinder (~30%), and Spirit Bonneville (30–40%) (Figure 6).

3. Far-Field Rock Distributions

3.1. Far-Field Rocks

After InSight landed, craters, rocks, and bedforms that could be identified in both the InSight panoramas and in HiRISE were identified (Golombek, Warner et al., 2020, Golombek, Williams et al., 2020). Golombek, Williams et al. (2020) further mapped 11 large rocks and 15 craters (1–10 m diameter) that could be confidently identified in both and included a HiRISE image georeferenced into a map view, showing the location of these features out to around 40 m distance from the lander. These same rocks and craters were also identified in eight ~45° views of the surface panorama. The azimuths of these features in the panoramas matched their azimuths in the HiRISE image to within 1°, indicating the spacecraft Inertial Measurement Unit that measured the yaw, pitch, and roll of the spacecraft to determine the site frame (with respect to north on Mars) was accurate within 1° as expected (Golombek, Williams et al., 2020). Herein, we have identified and mapped a total of 82 rocks that could be identified in both the HiRISE image (Figure 7) and the InSight panoramas (Figures 8–15), so as to better characterize the rock distribution over a broader area (out to ~40 m) from the lander. Because these rocks can be identified in the HiRISE image, their distance from the lander could be measured and their diameter and height could be determined from the size of the pixels in the panorama of the IDC at that distance.

3.2. Far-Field Rock Method

Relatively large rocks were identified in the afternoon and evening portions of the IDC panoramas that emphasized shadows. The relative distance of the rock was initially estimated qualitatively in the panorama by its position and size with respect to large rocks and craters that had already been identified (Golombek, Williams et al., 2020) (Figures 8–15). The azimuth of the rock was noted in the panorama and then the HiRISE image was inspected for circular to elliptical shadows that extended to the southeast, i.e., the perpendicular to the terminator, separating the illuminated rock face, at the relative distance estimated in the panorama. If a light-dark pattern of pixels (to northwest and southwest, respectively) was identified, the azimuth and relative distance were compared to that in the panorama. Finally, the location of the rock and its size had to match the azimuth (with the shadow extending to the southeast), relative distance, and size of other nearby surface features to be considered a match. Once the rock was identified on the HiRISE image, the azimuth and distance from the lander were measured. We used a sharpened, not map-projected HiRISE image (NO MAP, ESP_036761_1845) with a pixel resolution of 27.5 cm/pixel to avoid resampling pixels that was georeferenced into a map view (Figure 7).

To measure the size of the rocks, the IDC camera pixel scale of 0.82 mrad/pixel at the center of the image (Maki et al., 2018) was multiplied by the distance to the rock in meters to get the size of each pixel in mm. Rock height was measured by counting the number of pixels in a vertical column from the base to the top of the rock. The width of the rock was measured by counting the number of pixels across a horizontal row. The number of pixels was multiplied by the size of each pixel at that distance to get the width and height of each rock. Because the images of the rocks are oblique, only the side or sides facing the camera could be seen and so independent measurements of the length and width of the rocks could not be made. However, there is no reason that the orientation of the rocks viewed from the lander would have a preferred direction, so the observed apparent width can be considered as an average sample of the actual rock diameter. This is the same assumption for rock diameter measured from shadows in HiRISE images where the solar illumination direction is constant in the image and thus, the measured width of the shadow can be considered an average sample of the rock diameter (e.g., Golombek

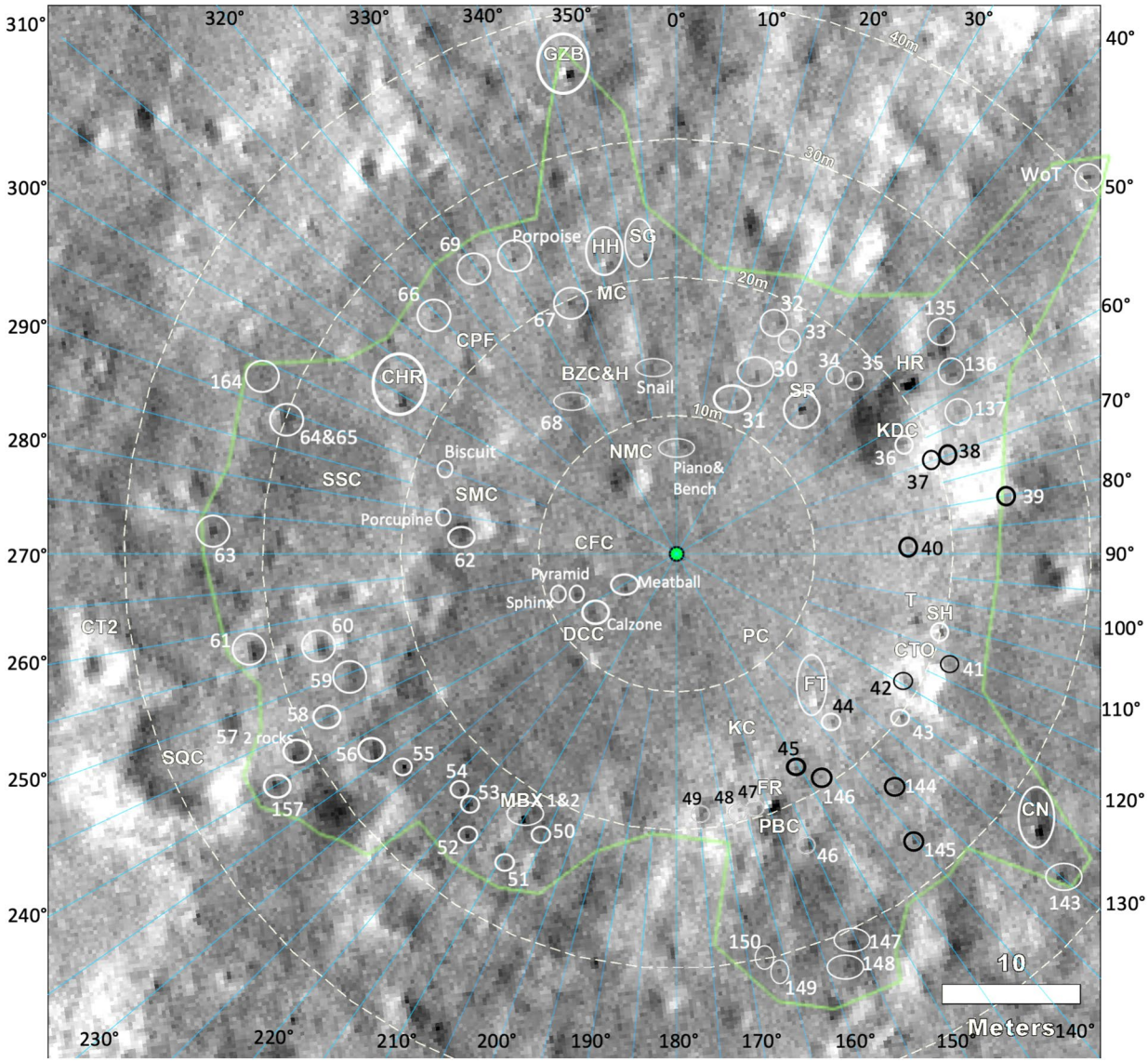

Figure 7. HiRISE image of the area around the InSight lander (green dot) with craters and rocks that can be identified in both the surface panoramas as well as this orbital image. Rocks are circled and either numbered or named (abbreviations) in Table 2, which includes the azimuth, distance, diameter, and height. These rocks are identified in the surface panoramas in the subsequent figures. The green line encloses area used to determine the SFDs. Outside black numbers are azimuths in degrees (blue lines every 5°) clockwise from north. Dashed white circles are distances from the lander in 10-m increments. Craters clockwise from due north (up on the image), abbreviations are: KDC is Knee Deep crater, CTO is Corintito crater, PC is Puddle crater, PBC is Peekaboo crater, KC is Kettle crater, DCC is Deep Cut crater, SQC is Squash crater, CT2 is Corintitwo crater, CFC is Coffee crater, SMC is Smudge crater, SSC is Sunset crater, CPF is Campfire crater, BZC&H is Blast Zone crater and hollow, NMC is Near Miss crater, and MC is Mole crater. Named rocks and craters from Golombek, Williams et al. (2020). HiRISE image number ESP_036761_1845 is not map projected at 27.5 cm/pixel, with the Sun 54° from vertical from the northwest, azimuth 293° measured clockwise from north, but has been georeferenced into a map view and is contrast enhanced to emphasize illuminated rock bright sides to the northwest and shadows in the solar azimuth to the southeast.

et al., 2008, Golombek, Huertas et al., 2012). As a result, we will assume that the measured apparent width is roughly the diameter.

There are 82 far-field rocks measured in this data set over a total area of 2630.38 m^2 (Figures 8–15, Table 2). Rocks measured range from 5–40 m away from the lander. Rock diameter varied from 0.1 m to 0.6 m and rock height varied from 0.1 m to 0.3 m. Roughly, one third of the rocks have diameters below the pixel scale of the HiRISE image (~0.3 m/pixel), indicating that the signal to noise of the HiRISE camera is sufficient to produce illuminated (bright)-shadow (dark) pairs that are as small as one pixel each. In general, far-field rocks are higher

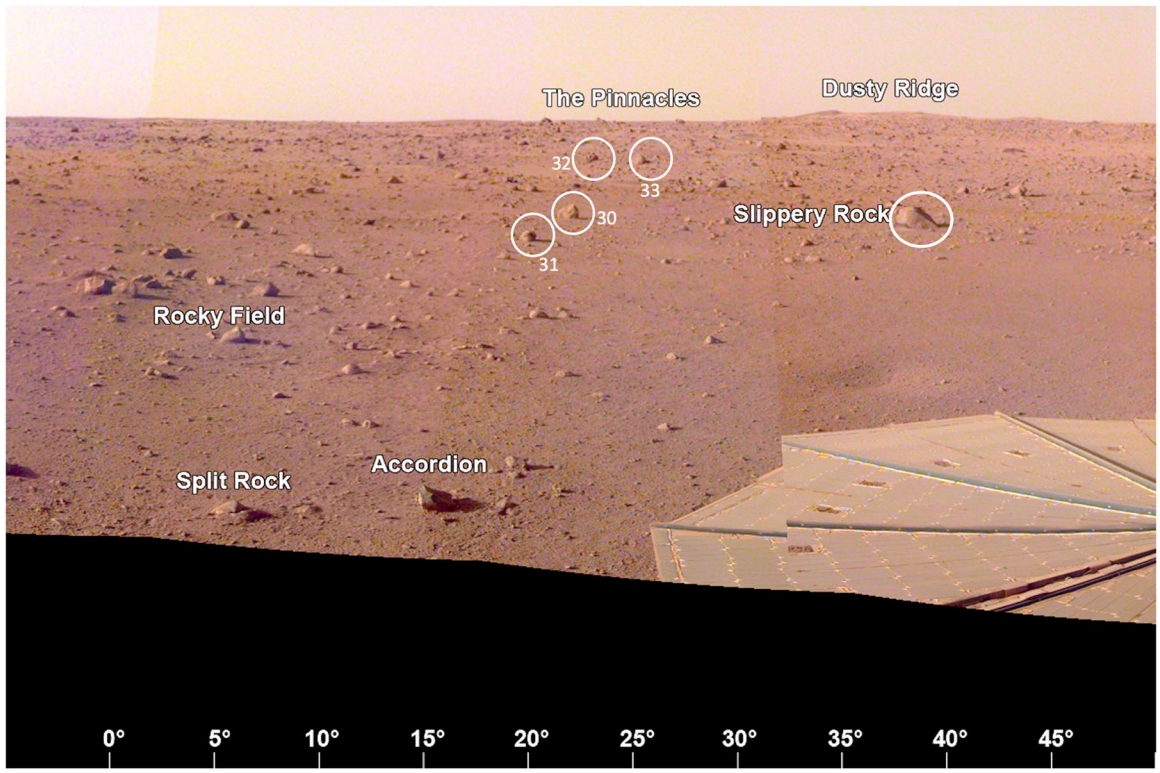

Figure 8. The view from the lander looking to the north-northeast (0° to 50°) showing measured rocks (circled, named, or numbered), part of the solar panel, Rocky field, the smooth terrain to the east (right), and rockier terrain outside *Homestead hollow*. On the horizon are The Pinnacles rocks (three) and Dusty ridge, an eolian bedform about 50 m away on the rim of a 100-m diameter degraded impact crater. A portion of the evening panorama has been stretched and is not true color.

than the usual hemisphere of one half the diameter, but this is not surprising as taller rocks are easier to see in distant oblique images and cast longer shadows in HiRISE images.

Uncertainties in the measurements are due to azimuthal uncertainties in the surface panorama, spatial and azimuthal uncertainties in the HiRISE image, and the camera pixel scale. Spatial uncertainties in the HiRISE image and azimuths in the surface panorama probably do not contribute as the HiRISE image was carefully georeferenced to a hierarchically georeferenced suite of decreasing resolution orthoimages and DEMs that control its spatial and azimuthal accuracy and comparisons with the controlled panorama show uncertainties in azimuth to less than 1° (Golombek, Williams et al., 2020 and Section 4). These uncertainties are only relevant to identifying the same rock in both images and measuring the distance to the rock and are probably small compared to the camera pixel scale. IDC pixels range in size from 0.5 cm to 3.3 cm and from 5 m to 40 m, respectively, so given that rock width and height can only be measured to ±1 pixel (e.g., Golombek et al., 2008), this is the uncertainty in the rock measurements. Far-field rocks are greater than 13 cm in diameter, so uncertainties of ≤3 cm will have no appreciable effect on the log-log plots of size-frequency distributions.

3.3. Far-Field Rock Size-Frequency Distribution

The SFD of the CFA versus diameter of rocks in the far field falls around the 3% model curve for diameters of 0.4 m to 0.9 m (Figure 16). At diameters below 0.4-m diameter, the slope of the SFD flattens considerably. This flattening of the SFD is likely due to resolution roll-off, where only some rocks of small size, which in this case are below the pixel scale of the HiRISE camera, are detected. This resolution roll-off is typical in HiRISE detections of rocks (Golombek et al., 2008, Golombek, Huertas et al., 2012) as well as in crater SFDs where the crater diameter approaches the resolution of the image. The far-field CFA SFD peaks just above the 3% model curve at almost the same maximum of ~3.2–3.5% CFA as the SFD of all rocks is measured in orthoimages within 10 m of the lander. The cumulative number of rocks per m^2 versus diameter plot for far-field rocks also falls on the same model curve as all rocks measured near the lander Figure 17. The similarity of the far field and nearby CFA (just

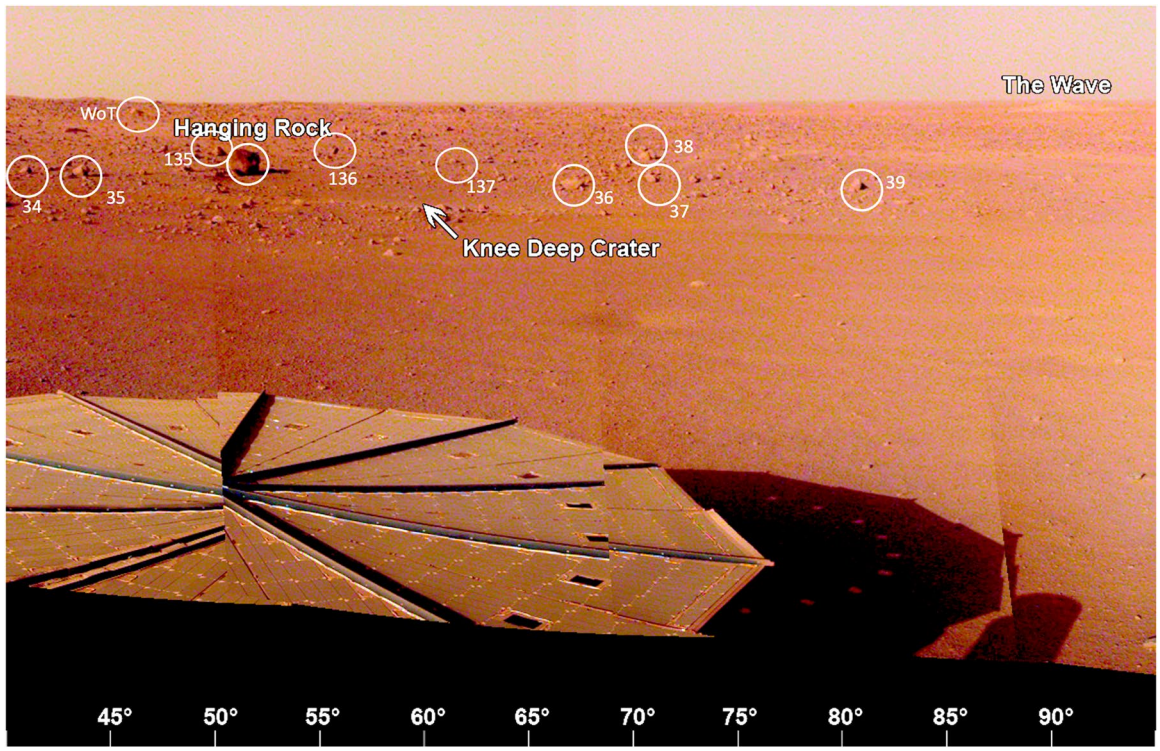

Figure 9. The view from the lander looking to the northeast-east (40° to 95°) showing measured rocks (circled, named, or numbered), craters, solar panel, and the smooth terrain of *Homestead hollow* out to around 15 m. The eolian bedform, The Wave is on the horizon around 400 m away to the east. A portion of the evening panorama has been stretched and is not true color.

above 3%) indicates that the rock distribution within 10 m of the lander is similar to that within around 40 m of the lander. For rocks whose diameter is at the pixel scale of HiRISE (27 cm), roughly 20% of the rocks expected for the 3% CFA distribution observed at larger diameters were detected using this method.

4. HiRISE Rock Distributions

During landing site selection, measurements of rocks in >50 HiRISE images derived via the rock machine vision shadow segmentation, analysis, and modeling method used for Phoenix and Mars Science Laboratory landing sites (Golombek et al., 2008, Golombek, Huertas et al., 2012) were used to measure the rocks in the InSight landing ellipse (Golombek, Kipp et al., 2017). Rock diameter and height were measured to ±1 HiRISE pixel (~0.3 cm, Golombek et al., 2008). Maps of rock abundance in 150 m by 150 m square areas (22,500 m^2) show that rocks are concentrated around sparse rocky ejecta craters (with up to 35% CFA), but are very low in between (1–2%). To compare the rock counts made from orbit to those made from the lander, all rocks detected in a 1-km-sided square centered on the lander (312) were plotted. However, because detections include false positives (scarps, hills, and eolian bedforms) that were generally >2.25 m diameter, the estimate of rock abundance made prior to landing was based on rocks 1.5–2.25 m diameter (Golombek, Huertas et al., 2012, Golombek, Kipp et al., 2017).

To remove false positives, we selected detections that were confirmed by a human who mapped rocks, craters, and eolian bedforms in a HiRISE orthoimage (ESP_036761_1845 at 25 cm/pixel) and the 1-m elevation posting DEM (created from ESP_036761_1845 and ESP_037262_1845, designated as InSightE17_C by Fergason et al., 2017). A total of 7069 rocks were mapped by human detection within a 2.25-km^2 area surrounding the landing site. Rocks that are >2 to 4 HiRISE pixels in diameter (0.5 cm–1 m) form obvious, circular to elliptical shadows that extend to the southeast (solar illumination from the northwest at 54° from vertical) in the opposite direction of the illuminated rock face. This illumination pattern is distinguishable from small, meter-size craters that cast arcuate illuminated rims toward the northwest and corresponding shadows to the southeast (if a prominent rim is present). Each identified rock was marked in ArcGIS with a single point based on these criteria. No

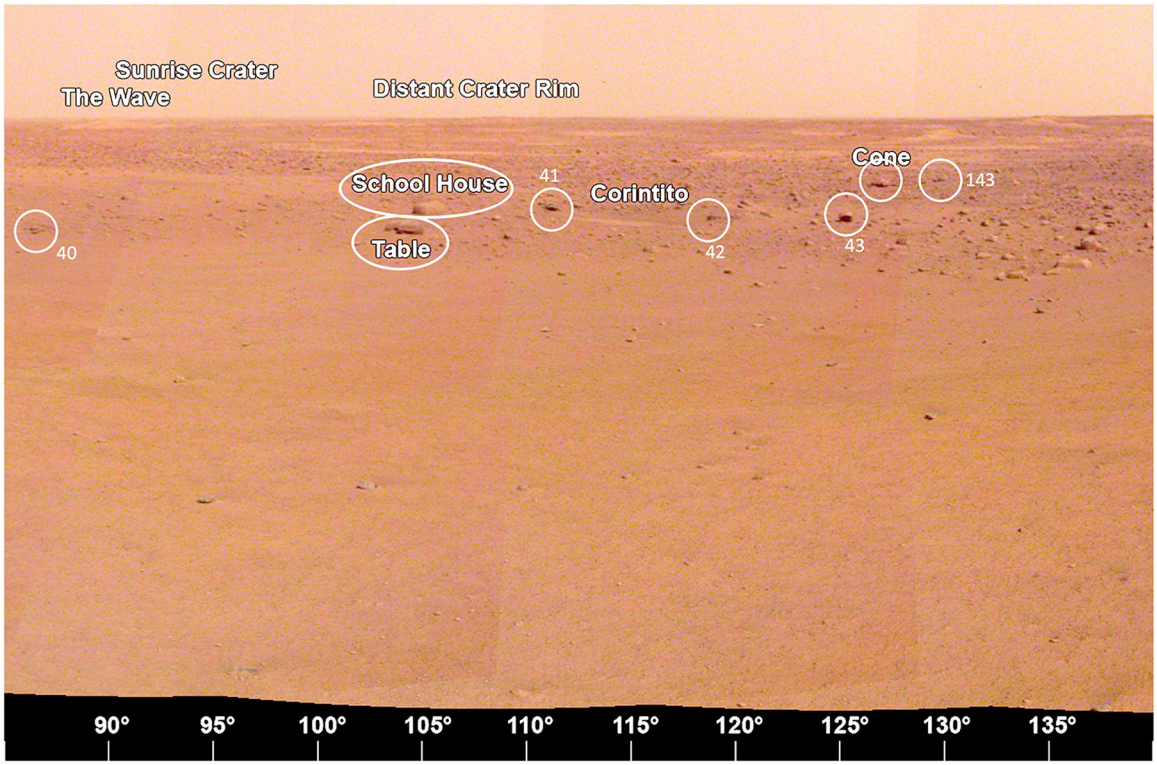

Figure 10. The view from the lander looking to the east-southeast (90° to 140°) showing the measured rocks (circled, named, or numbered) and smooth terrain of *Homestead hollow* out to around 15 m. Note Corintito crater (a Corinto secondary crater in view, Golombek, Kipp et al., 2017; Golombek, Warner et al., 2020) is about 20 m away. In the distance, The Wave, a bright eolian bedform, and the Sunrise crater rim are on the horizon around 400 m away. The rim of a larger (460 m diameter), relatively fresh Distant crater, can be seen on the east-southeast horizon ~2.4 km away. A portion of the afternoon panorama has been stretched and is not true color.

attempt was made to digitize the areal extent of each rock or measure their diameters. The map area was subdivided into 0.3 km by 0.3 km grids to ensure complete mapping coverage.

The machine vision rock detection algorithm using shadows is performed on non-map projected HiRISE images (NOMAP). Map-projected HiRISE images have resampled pixels to a constant 25 cm/pixel, which can blur the edges of shadows. As a result, rock detections based on shadow segmentation in NOMAP images (to avoid resampled pixels) had to be georeferenced to the map-projected version of the HiRISE image and the orthophoto used for the human mapping. The NOMAP image (ESP_036761_1845_RED.NOMAP.tif) was georeferenced to the map-projected HiRISE visible image using 66 tie points and rubber sheet links between the source points in the NOMAP image and the target points in the map-projected HiRISE image. A linear spatial adjustment was performed using these rubber sheet links, allowing the rocks to be transformed into the map-projected HiRISE image. After georeferencing, rocks in the HiRISE image were within 0.5 meters of their original location in the NOMAP image. In order to match rock detections in the map-projected HiRISE image, a spatial join was executed by searching within a 1.5-m radius of each rock point. Rock features within a 1.5-m radius of each other were linked as the same rock.

Figure 18 shows 3397 rocks mapped by a human and the confirmed machine vision rocks (172). These rocks are between 0.4 m and 2 m in diameter and the majority of them are located around three rocky ejecta craters (Golombek, Kass et al., 2020). Of these, the 100-m diameter Sunrise crater is the freshest and is about 400 m to the east-southeast (Figure 18). Other detected rocks including those around the lander are not obviously related to the rocky ejecta craters (Grant et al., 2020).

The SFDs of the confirmed machine vision rocks are plotted in Figures 16 and 17. The CFA versus diameter SFD (Figure 16) for rocks >1.6 m–2 m diameter is parallel to the 5% exponential model distribution. The CFA SFD for rocks 1.6-1.2 m diameter is parallel to the 4% exponential model distribution. The SFD of rocks smaller than 1.2-m diameter shallows relative to the exponential model curves similar to most HiRISE counts, which is due

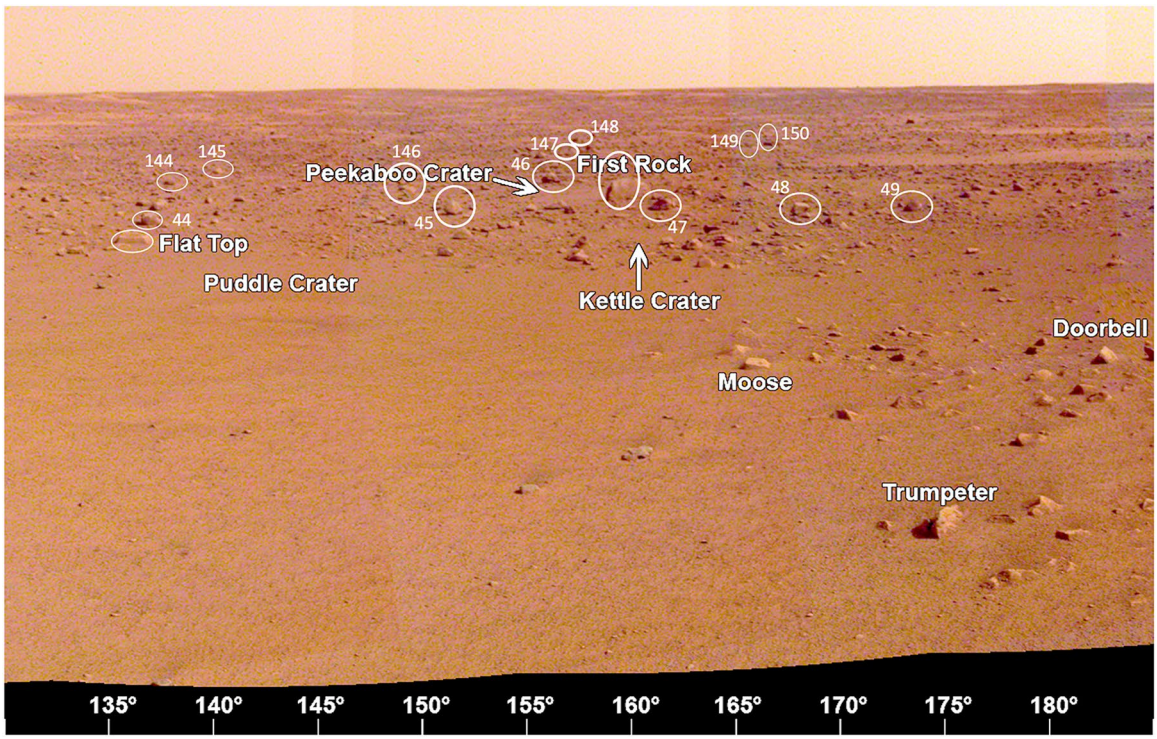

Figure 11. The view from the lander looking to the southeast-south (130° to 185°) showing measured rocks (circled, named, or numbered), craters, and the smooth terrain of *Homestead hollow* with the rockier terrain beyond. A portion of the afternoon panorama has been stretched and is not true color.

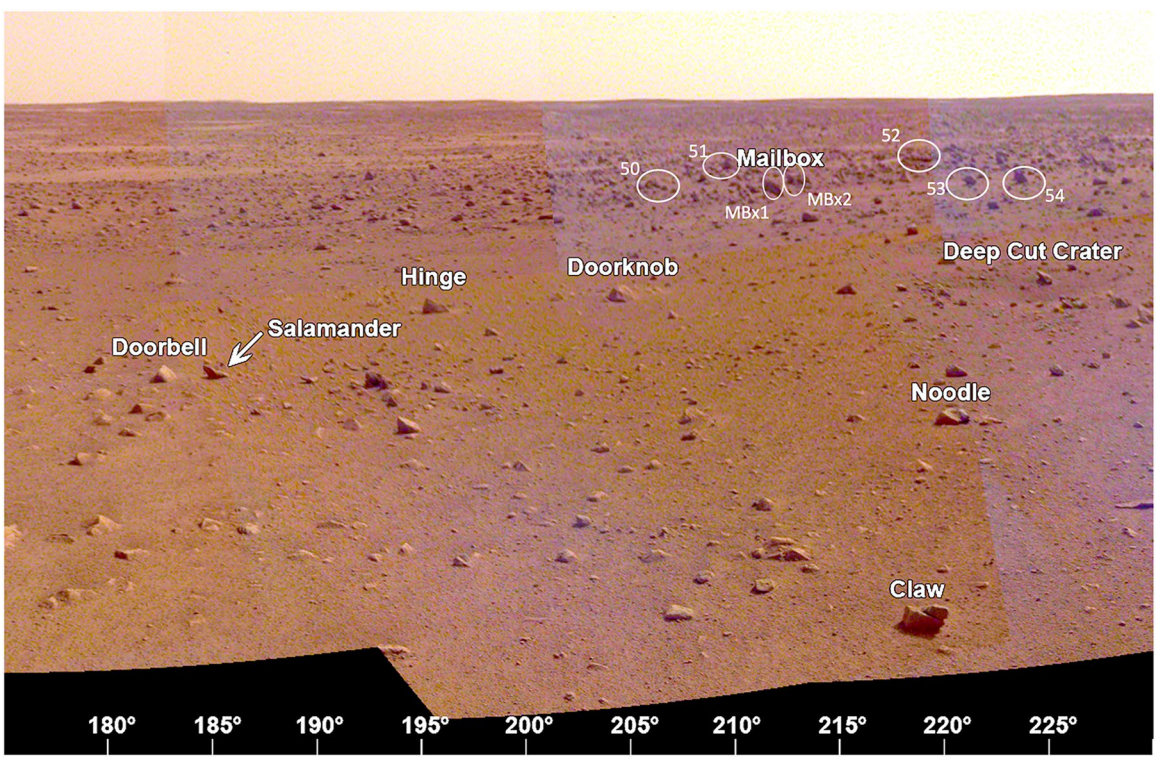

Figure 12. The view from the lander looking to the south-southwest (175° to 230°) showing measured rocks (circled, named, or numbered), craters, the rockier terrain of *Homestead hollow,* and the rockier terrain outside the crater. A portion of the afternoon panorama has been stretched and is not true color.

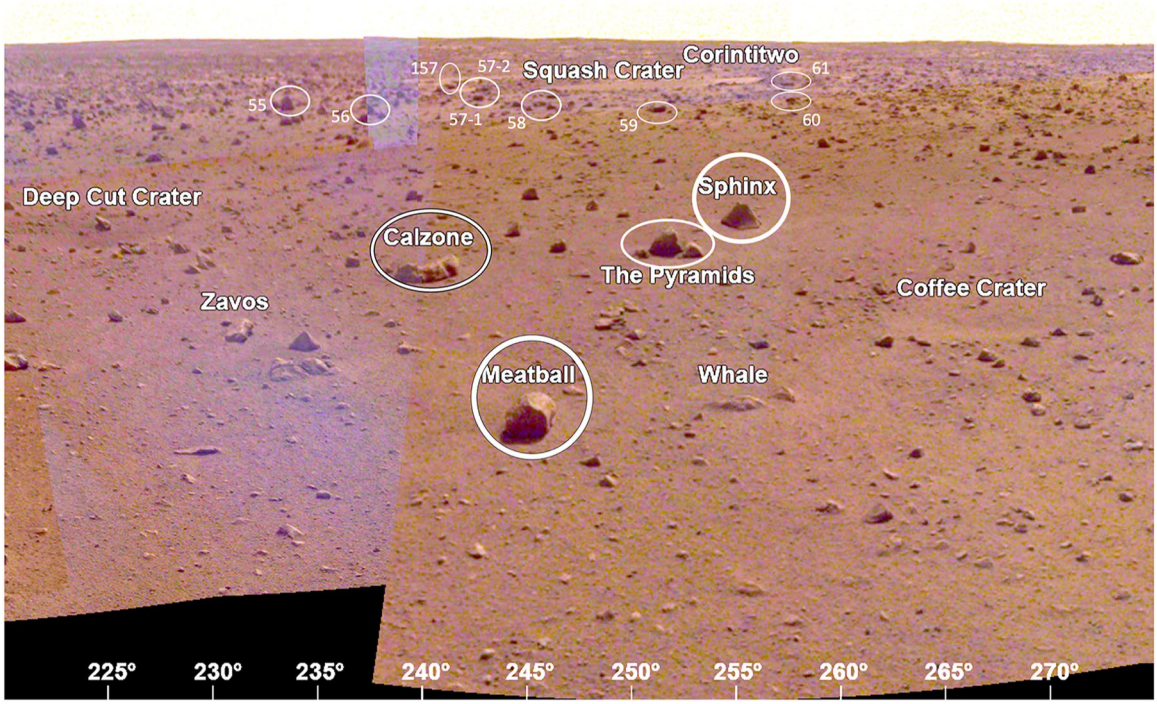

Figure 13. The view from the lander looking to the southwest-west (220° to 275°) showing measured rocks (circled, named, or numbered), craters, the rockier terrain of *Homestead hollow*, and the indistinct rim. Note Corintitwo crater (a Corinto secondary crater in view, Golombek, Kipp et al., 2017, Golombek, Warner et al., 2020) is about 40 m away. A portion of the afternoon panorama that has been stretched and is not true color.

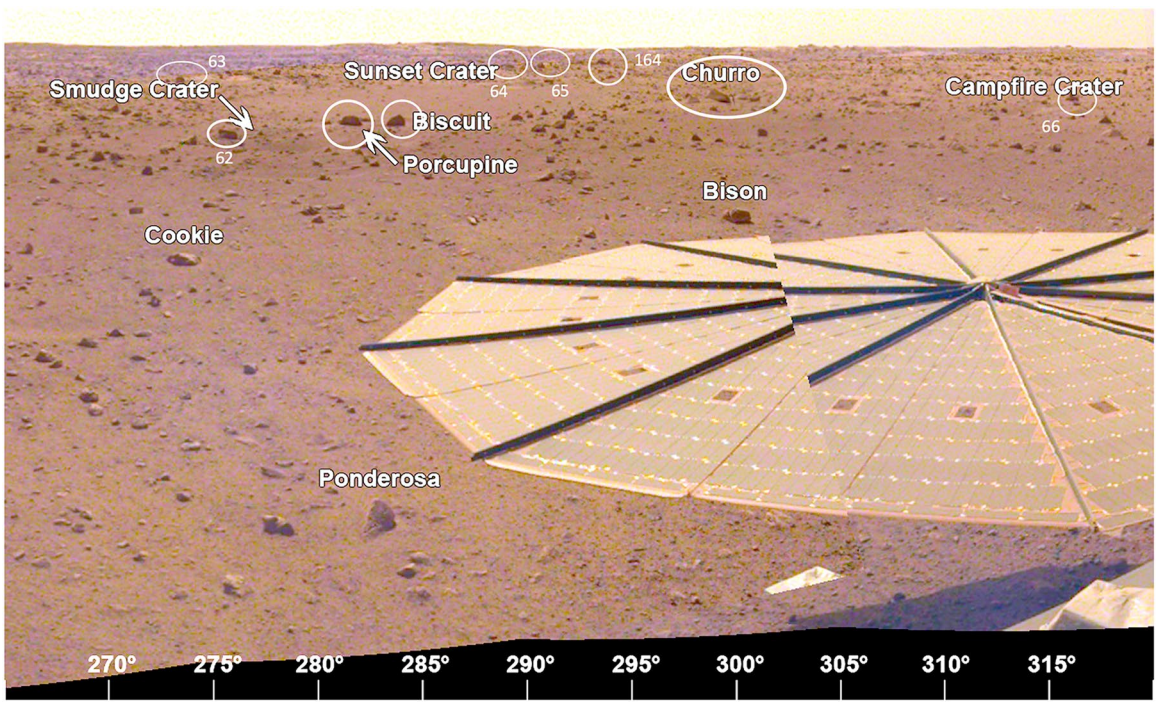

Figure 14. The view from the lander looking to the west-northwest (265° to 320°) showing measured rocks (circled, named, or numbered), the solar panel in the foreground and the rockier terrain of western *Homestead hollow*. Note Sunset, Smudge, and Campfire craters. A portion of the afternoon panorama that has been stretched and is not true color.

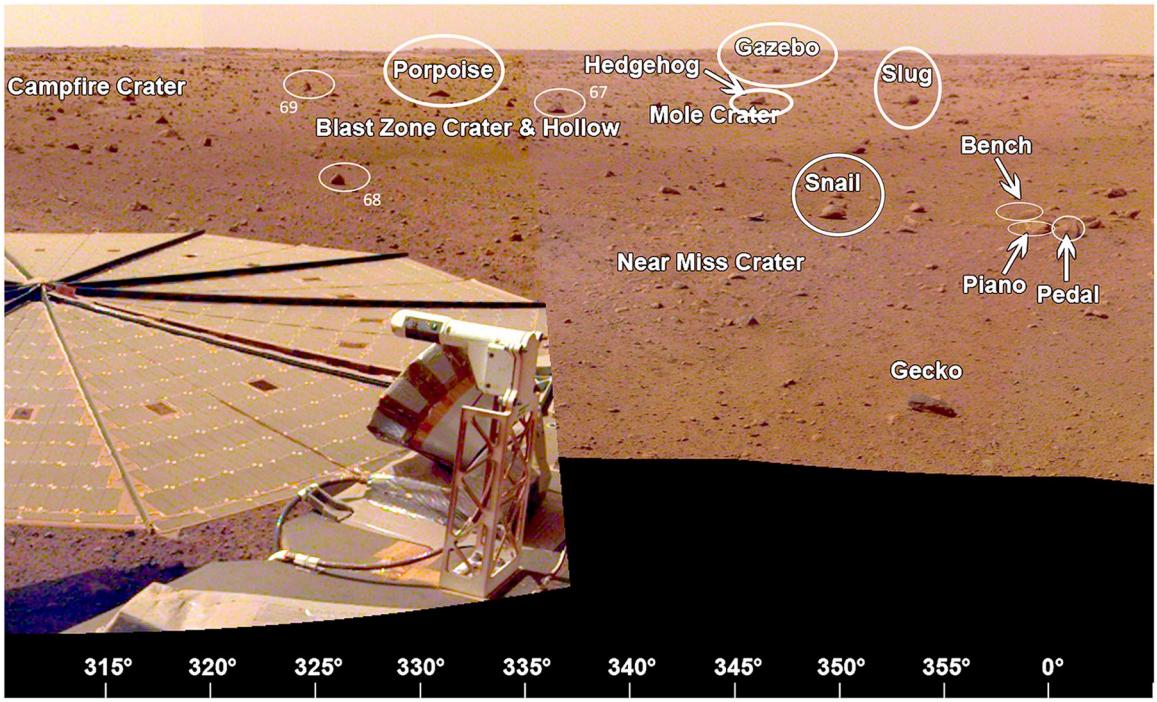

Figure 15. The view from the lander looking to the northwest-north (310° to 0°) showing measured rocks (circled, named, or numbered), craters, the solar panel, the rockier terrain of *Homestead hollow*, and several small craters. Also note a meteorology mast. A portion of the afternoon panorama that has been stretched and is not true color.

to resolution roll-off in which rocks with fewer than 5 pixels are detected less frequently (Golombek et al., 2008, Golombek, Huertas et al., 2012). The SFDs for the cumulative number of rocks per m^2 (Figure 17) show similar relationships.

The 4–5% rock abundance indicated by the HiRISE detections from orbit is 1–2% higher than rocks measured near the lander and in the far field. It does match the 4–5% of the rockier areas to the north and west of the lander. Counts of rocks in 150 m square tiles (22,500 m^2 area) used to estimate the CFA (Golombek, Kipp et al., 2017) show that although the area within a few hundred meters has low rock abundance (1–2%), rocky ejecta craters within 0.5 km (Figure 18) produce a spike in rock abundance (Golombek, Kass et al., 2020) that appears responsible for the measured 4–5% rock abundance.

As a result, the rock abundances observed from orbit fall on similar exponential model rock abundance curves as those viewed from the surface. Therefore, InSight joins Viking Lander 1 and 2, Mars Pathfinder, Phoenix, and Spirit landing sites where rock counts in HiRISE images fall on the same exponential model curve as those seen from the surface (Golombek et al., 2008, Golombek, Huertas et al., 2012). The measurements further strengthen the use of HiRISE images to measure rocks, fitting these rocks to an exponential SFD model and extrapolating along the model to predict the number of rocks smaller than 1.5 m that could be potentially hazardous to landing spacecraft (Golombek et al., 2008, Golombek, Huertas et al., 2012, Golombek, Kipp et al., 2017).

The average rock abundance of 4–5% (CFA) in the 1-km^2 area around the lander is consistent with thermal imaging estimates over larger pixel areas for the location of the lander. The InfaRed Thermal Mapper (IRTM) rock abundance in the 60-km pixel that contains the lander is 4% (Christensen, 1986). The nearest 7.5-km pixel Thermal Emission Spectrometer (TES) rock abundance estimate, about 10 km to the east, is 3.3% (7.5-km pixel) (Nowicki & Christensen, 2007), and the average TES rock abundance within 20 km of the lander is 3.7% (11 pixels). No TES rock abundance pixel includes the lander.

Table 2
Azimuth, Measured Clockwise From North in HiRISE, Distance Measured in HiRISE, Apparent Diameter, and Height of Rocks in the Far Field

Rock name and abbreviation	Azimuth in HiRISE (deg)	Distance in HiRISE (m)	Apparent diameter (m)	Height (m)
Piano Rock	0	8.5	0.18	0.14
Bench Rock	0	8.5	0.21	0.08
Pedal Rock	1	8.5	0.21	0.14
31	22	14.7	0.23	0.16
32	24	21.4	0.2	0.19
30	25	16.7	0.35	0.24
33	28	21.1	0.24	0.15
Slippery Rock, SR	40	13.8	0.55	0.32
34	41	20.2	0.24	0.14
35	45	22.6	0.32	0.26
WoT Rock	47	44.8	0.44	0.3
135	50	29.7	0.38	0.22
Hanging Rock, HR	53	20.7	0.59	0.52
136	57	29.2	0.13	0.13
137	63	28.4	0.26	0.17
36	64	25.8	0.52	0.32
37	69	26.4	0.36	0.29
38	69	27.7	0.53	0.29
39	83	26	0.4	0.3
40	88	23.3	0.23	0.17
Table Rock, T	106	17.6	0.4	0.22
School House Rock, SH	107	19.6	0.53	0.19
41	112	27.7	0.39	0.26
42	119	25.1	0.34	0.11
43	125	25.9	0.35	0.19
Cone Rock, CN	128	32.8	0.58	0.34
143	130	42	0.47	0.18
44	136	21.9	0.34	0.27
144	136	28.6	0.3	0.21
Flat Top Rock, FT	138	14.8	0.52	0.1
145	140	31.8	0.23	0.18
146	146	23.7	0.17	0.15
45	150	22	0.41	0.32
46	155	27	0.43	0.23
147	155	34.5	0.32	0.21
148	157	35.7	0.22	0.18
First Rock, FR	160	19.4	0.78	0.41
47	162	22.7	0.59	0.28
149	166	33.7	0.25	0.12
48	167	22	0.35	0.24
150	167	32.7	0.32	0.16

5. Comparison of Rocks Measured on the Surface and From Orbit

Four rocks observed from the lander were also detected by the machine vision rock detection algorithm in the HiRISE image. The rocks mapped in the far field, Hanging rock (Figure 9), First rock (Figure 11), Gazebo rock (Figure 15), as well as the easternmost of the three Pinnacle rocks (Figure 8) were detected and counted using the standard machine vision algorithm (Golombek, Kipp et al., 2017). The rock detector employs a modified maximum entropy thresholding technique using a nonlinear image stretching routine that segments shadows cast by rocks from non-shadowed pixels and fits ellipses to shadows and cylinders to the rocks (Golombek et al., 2008). Deconvolution methods are used to sharpen the images, detect smaller rock shadows, improve shadow segmentation, and differentiate and eliminate shadows not produced by rocks (Golombek, Huertas et al., 2012).

Subsequent methods developed for the Mars 2020 Rover landing site selection (Golombek, Otero et al., 2017) were used to systematically vary these parameters to detect a larger sample of possible rocks that were used to define safe areas for landing. Different combinations of three parameters and two sharpening techniques were iterated through a series of runs and combined to maximize the number of rocks that could be detected. Gamma, a parameter which enhances shadow intensity, mean gradient threshold, a parameter which is used to determine the edge of a shadow by comparing a shaded region to its background, shadow aspect ratio, which is the ratio of a shadow length-to-width used to remove false positives like eolian bedforms, and normalizing the image to remove common background signal were all varied. After these parameter sweeps (a total of 168 runs), clusters of overlapping "duplicate" detections were identified as groups of rocks within 7 cumulative pixels of each other using rock position and diameter. Each cluster of "duplicate" detections was replaced with a rock that was averaged from all of the detections. Hanging rock (Figure 9) was measured using this method.

These four rocks detected in the HiRISE image vary in distance from the lander from 19 m to 60 m and are shown in Figure 18 (three of them are shown on Figure 7). These rocks are the largest rocks (diameter and height) observable from the lander (diameters 0.6-0.8 m; heights 0.3-0.5 m) and thus cast the largest shadows. Table 3 shows the diameters and heights derived from the measurements in the surface panoramas (Section 3.2) and in HiRISE. The difference in diameter between the two methods is less than 0.03 m and the difference in heights between the two methods is 0.09 m. The difference in diameter is less than 5%; the difference in height is less than 23%. Previous tests of the performance of the rock detector on spacecraft of known size on the surface of Mars show that the algorithm accurately determined spacecraft diameter and height to within 1–2 pixels, which is about the limit of what could be expected (Golombek et al., 2008; Golombek, Huertas et al., 2012). The differences in height and diameter of the four rocks measured here are a small fraction of one pixel (27.5 cm/pixel in the NO MAP HiRISE image ESP_036761_1845), which further documents the excellent signal to noise of the HiRISE camera and the performance of the rock detection and measurement algorithm.

Table 2
Continued

Rock name and abbreviation	Azimuth in HiRISE (deg)	Distance in HiRISE (m)	Apparent diameter (m)	Height (m)
49	175	21.3	0.35	0.25
50	206	21.4	0.27	0.12
51	209	23.7	0.27	0.14
Mailbox 1 Rock, MB-1	212	22.2	0.41	0.27
Mailbox 2 Rock, MB-2	212	22.2	0.34	0.18
52	217	22.7	0.49	0.11
53	219	20.7	0.23	0.17
54	223	20	0.23	0.17
55	232	20.8	0.24	0.21
Calzone Rock	236	8.1	0.4	0.13
56	237	21.7	0.25	0.14
Meatball Rock	240	5.1	0.21	0.13
157	240	28.5	0.3	0.13
57-1	242	26.3	0.21	0.11
57-2	242	26.3	0.24	0.11
58	245	23.8	0.21	0.11
Pyramid 1 Rock	248	9.6	0.12	0.07
Pyramid 2 Rock	248	9.6	0.26	0.22
Pyramid 3 Rock	248	9.6	0.17	0.11
59	249	19.6	0.28	0.19
Sphinx Rock	250	9.6	0.29	0.21
60	255	20.7	0.19	0.09
61	257	25.3	0.25	0.07
63	272	27.2	0.23	0.15
62	274	9.2	0.17	0.06
Porcupine Rock	279	10.7	0.21	0.09
Biscuit Rock	283	17.9	0.3	0.17
64	290	23.8	0.16	0.12
65	290	23.8	0.22	0.11
164	293	26.1	0.3	0.14
Churro Rock, CHR	299	22.8	0.47	0.25
66	315	19.5	0.18	0.15
Porpoise Rock	331	24.4	0.46	0.14
69	340	21.4	0.17	0.17
Hedgehog Rock, HH	347	21.5	0.32	0.19
Gazebo Rock, GZB	347	35.4	0.59	0.31
Slug Rock, SG	354	21.6	0.61	0.28
68	355	10.5	0.15	0.11
67	356	17.8	0.29	0.17
Snail Rock	356	13.5	0.33	0.21

Note. Large, named rocks from (Golombek, Williams et al., 2020).

6. Fragmentation

The SFD of rocks measured from both the lander and orbit is consistent with estimates made from fragmentation theory prior to landing (Golombek, Kipp et al., 2017). Fragmentation theory (Charalambous, 2014) was used to model the particle size-frequency distribution of the regolith (including the rock abundance) based on the rocks and craters measured in HiRISE images, and negative binomials were fit to all rocks measured in the landing ellipse (Golombek, Kipp et al., 2017). These fits are similar to the Phoenix and Spirit landing site rock size-frequency distributions for diameters smaller than about 1 m (Golombek, Kipp et al., 2017, Golombek, Kass et al., 2020). In this section, we explore this further using the near-field, far-field, and HiRISE rock counts.

Based on the probabilistic calculation of repeated fracture of a particle population, the fragmentation theory developed by Charalambous (2014) allows an understanding of the time-dependent processes that formed an observed rock population. Under repeated fracture events, the ensemble of these fragmentation processes can be described by a negative binomial (NB) function in which the rock-size distribution evolves over time at different rates according to the maturity index, t (number of fragmentation events) and a probability of fracture, p. For the larger fragments on Mars (diameter > ~1 mm), the maturity index is dominantly determined by the number of meteorite impacts, which is constrained by the age of the surface and the crater population. For smaller fragments (d < ~1 mm), the maturity index and the probability of fracture become increasingly determined by the activity of eolian processes, which contribute to the evolution of a grain distribution, most notably from the processes of saltation for sand-size particles, to creep for granule-size particles (Golombek et al., 2018; Golombek, Charalambous, 2020).

The NB fit for the InSight rock data was made to restricted portions of the three rock SFDs (Figure 19) to avoid the resolution roll-off of the data where the image resolution resulted in fewer rocks measured (discussed earlier for each data set) and the SFDs shallow. As a result, rocks with diameters below 1.2 m were omitted from the HiRISE data and those with diameters below 0.3 m diameter were omitted from the far-field data (roughly where the far-field SFD crosses the near-field SFD). The three InSight rock distributions fit an estimated maturity index of $t = 3.3 \pm 0.3$ (Figure 19), and fall within the error bounds of initial predictions made just from particle size measurements of InSight's workspace (Charalambous et al., 2019), rocks measured in HiRISE images in the landing ellipse, and the measured crater population (Golombek, Kipp et al., 2017). Given the NB statistics, the observed rock population is estimated to be the product of ~3 fragmentation events, or impacts, on average. This means that the fragmentation model indicates that the rock population has experienced approximately 3.3 self-similar and scale-invariant fragmentation events that have produced the observed and measured rock distribution. The measured rocks are the product of impacts that excavated bedrock, subsequent impacts that fragmented this material, and any thermal cracking. The NB curve is consistent with the 5% exponential rock model curve matching the HiRISE rock counts for diameters greater than 1.6 m and falls between the 4% and 5% exponential model curves for smaller diameters.

NB fits for rock populations at other landing sites on Mars (Spirit, Phoenix, Viking Landers and Mars Pathfinder) share a common relatively high probability of fracture (p = 0.75, Golombek et al., 2017), indicative of the

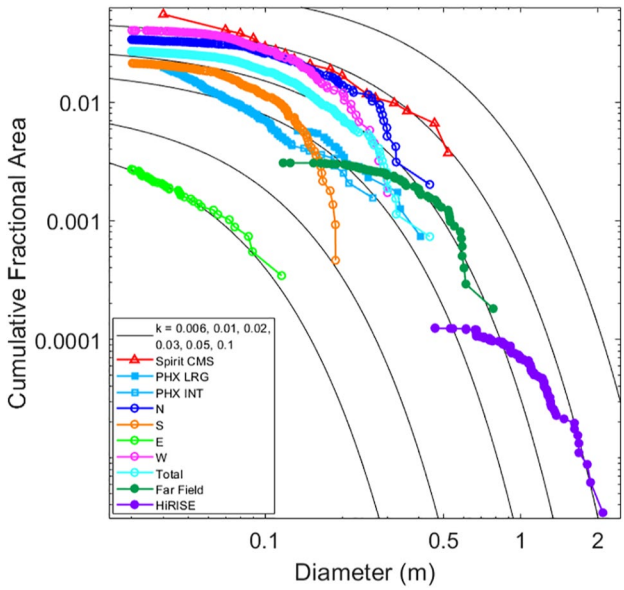

Figure 16. Cumulative fractional area versus diameter plot of rocks around the InSight lander within 10 m (near field), within 40 m (far field), and in HiRISE. Areas within 10 m around the lander are: North (N), South (S), East (E, *Homestead hollow*), West (W), and all areas combined (total). Also shown are the Phoenix (Heet et al., 2009; Golombek, Huertas et al., 2012) and Spirit landing site (Golombek et al., 2006) rocks, rocks detected in HiRISE, and exponential model curves for 0.6%, 1%, 2%, 3%, 5%, and 10% rock abundance (Golombek & Rapp, 1997). Confirmed HiRISE rocks measured in a 1-km^2 area around the lander are shown in Figure 18.

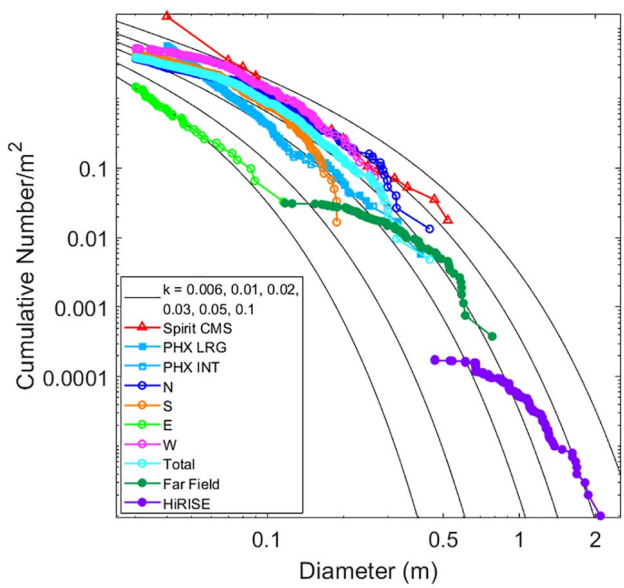

Figure 17. Cumulative number per m^2 versus diameter of rocks within 10 m of the lander (near field), in the far field (within 40 m), and in HiRISE. Also shown are the Phoenix (Heet et al., 2009; Golombek, Huertas et al., 2012) and Spirit landing site (Golombek et al., 2006) rocks, and equivalent exponential model curves for 0.6%, 1%, 2%, 3%, 5%, and 10% rock abundance (Golombek & Rapp, 1997; Golombek, Haldemann et al., 2003). Confirmed HiRISE rocks that are plotted were measured in a 1-km^2 area around the lander shown in Figure 18.

same underlying processes of fragmentation by impacts. Shown in Figure 19 are NB fits to the measured surface rock SFDs at the Spirit and Phoenix landing sites (Golombek, Kipp et al., 2017). Both of these landing sites have the nearest rock SFDs to InSight with close-to-parallel slopes to InSight's NB fit for total rock counts measured from both orbit and surface cameras. The NB fit of the InSight rock abundance appears higher than the Phoenix NB fit, but lower than the Spirit landing site. The close match to the Spirit landing site is consistent with both predictions prior to landing (Golombek, Kipp et al., 2017) and the appearance as well as similar geological history of the two sites (impacted Hesperian/Amazonian lava flows, Golombek, Kass et al., 2020). The similar multiplicity effect of the NB statistics from multiple fragmentation events (here at $t = 3.3$) is suggestive of an impact-comminuted rock population rich in sand-sized material (Golombek, Charalambous et al., 2018, 2020), consistent with orbital thermal inertia measurements and the low rock abundance at the landing site (Golombek, Kass et al., 2020). The observation that Amazonian impact cratering of hard, relatively intact bedrock (basalt) can produce a meters-thick surface layer with low rock abundance that is dominated by sand-sized particles (at both the Spirit and InSight landing sites, Golombek et al., 2006; Golombek, Warner et al., 2020) suggests that the global surface layer composed of mostly fine-grained materials on Mars (Christensen & Moore, 1992) is produced mainly by impact and eolian processes (e.g., Golombek, Charalambous et al., 2018, 2020).

7. Summary and Conclusions

Rocks around the InSight lander in the near-field, far-field, and in a HiRISE orbital image were measured to produce rock size-frequency distributions (SFD), representing the first full treatment of this type for this landing site. More than 2,000 rocks were counted in four areas from an orthomosaic produced from 283 IDC images within 10 m of the lander. The SFDs of the four areas are similar to exponential model SFD curves, developed from the Viking Lander 1 and 2 rock SFDs for rock abundances of <1% to ~5%. Altogether, the SFD of the entire near field has a cumulative fractional area (CFA) of ~3% in between the ~2% rock abundance at the Phoenix and 5% rock abundance at the Spirit landing sites. The curved shape of the SFD of the InSight near-field rocks is also similar to other landing sites on Mars as well as the exponential model curves and are not straight line power law SFDs.

Rocks within 40 m of the lander that could be identified in both the surface, controlled panorama, and in a sharpened NOMAP HiRISE image were also measured by determining their distance in HiRISE and their size from the IDC pixel scale. Eighty-two far-field rocks 0.1–0.6 m diameter were measured. The illuminated and shadowed portions (bright-dark pixel pairs) of rocks could be identified even if the rocks are smaller than the HiRISE pixels, likely a result of the excellent signal to noise of the HiRISE camera. The SFD of the CFA versus diameter of rocks in the far field follows the ~3% model curve for diameters of 0.4 m to 0.9 m, which is the same model curve for all near-field rocks with diameters of 0.03–0.4 m.

Rocks measured with the machine vision rock detection algorithm used to determine rock abundance during landing site selection and verified by a human within a 1-km^2 area centered on the lander are parallel to exponential model curves for 4%–5% rock abundance for rocks 1.2–2.0 m diameter. This CFA SFD is similar to the rock abundance of rockier areas in the near field to the north and west of the lander and is within 1%–2% of the average

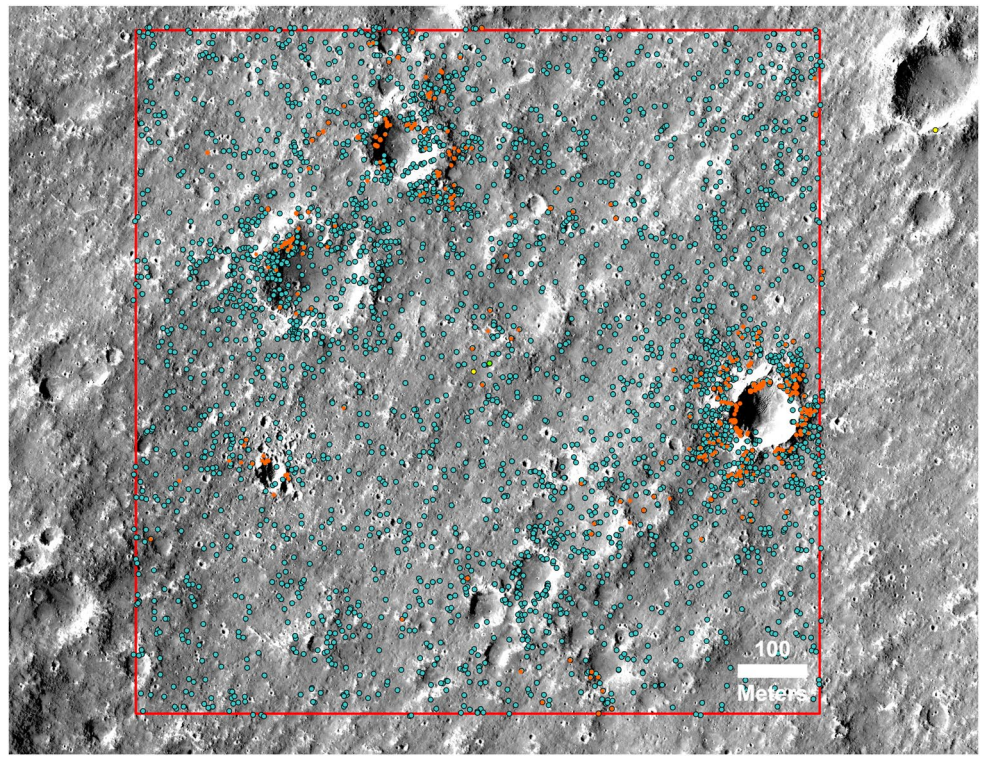

Figure 18. Rocks identified in HiRISE image in 1-km-sided square centered on the InSight lander (yellow dot). Blue dots are rocks identified by a human as described in the text. Orange dots are the machine vision detected rocks (Golombek, Kipp et al., 2007; Golombek, Kass et al., 2020) that have been confirmed by a human. Light green rock is Hanging rock (21 m to the northeast at 53° azimuth, measured clockwise from north), that was detected by varying parameters to detect a larger number of rocks. E Pinnacle (60 m to the northeast at 28° azimuth), First (19 m to the southeast at 160° azimuth), and Gazebo (35 m to the northwest at 347° azimuth) rocks are the three orange rocks closest to the lander (see Figure 7 and Table 3). Note rocky ejecta craters with concentrations of rocks.

near-field and far-field rock abundances. As a result, the rock abundances observed from orbit fall on similar exponential model rock abundance curves as those viewed from the surface, similar to the Viking Lander 1 and 2, Mars Pathfinder, Phoenix, and Spirit landing sites. This further strengthens the use of HiRISE images to measure rocks, fitting these rocks to an exponential SFD model and extrapolating along the model to predict the number of rocks smaller than 1.5 m that could be potentially hazardous to landing spacecraft. Rock abundance measurements at the InSight landing site are also consistent with thermal imaging estimates over larger pixel areas for the location of the lander. Four rocks detected and measured in the machine vision algorithm of the HiRISE image that could be measured from the lander have diameters (0.6–0.8 m) that agree within 5% and heights (0.3–0.6 m) that agree to within 23%, all within a fraction (<10%) of a HiRISE pixel.

Table 3
Comparison of Diameter and Height of Rocks Ddetected by the Machine Vision Algorithm in the HiRISE Image and in IDC Images of the Far Field From the Lander

Rock name	HiRISE diameter (m)	Far-field diameter (m)	Diameter difference (m)	HiRISE height (m)	Far-field Height (m)	Height difference (m)
Pinnacle E Rock[a]	0.58	0.60	0.02	0.30	0.28	0.02
Hanging Rock	0.58	0.59	0.01	0.41	0.52	0.09
First Rock	0.81	0.78	0.03	0.32	0.41	0.09
Gazebo Rock	0.59	0.59	0.004	0.32	0.31	0.01

[a]At a distance of 60 m and an azimuth of 28°.

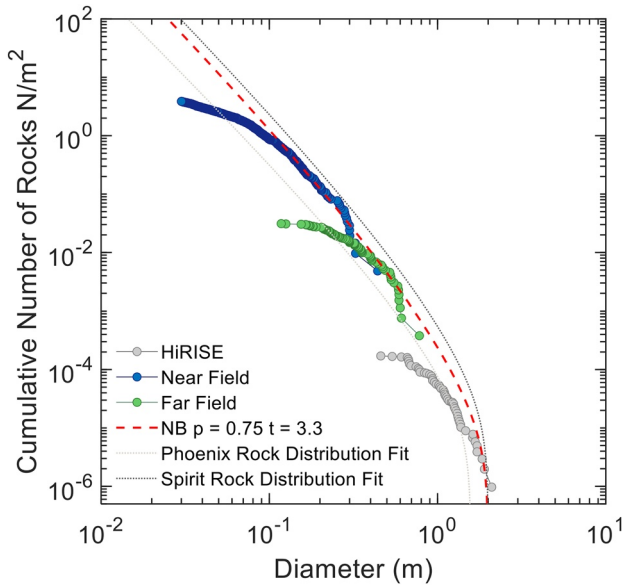

Figure 19. Cumulative number of rocks per m^2 versus diameter for the near and far fields and in HiRISE. Based on the fragmentation model of Charalambous (2014), the red-dashed line indicates the NB fit (p = 0.75, t = 3.3) to the compilation of all rock counts measured at InSight. The dotted lines represent the NB fits to the Spirit and Phoenix landing sites (Golombek, Kipp et al., 2017), shown here for comparison.

The SFD of rocks measured from both the lander and orbit is consistent with estimates made from fragmentation theory used to model the particle size-frequency distribution based on the rocks and craters measured in HiRISE images. A negative binomial (NB) function based on the number of fragmentation events and the probability of failure was fit to near-field, far-field, and HiRISE-measured SFD of rocks (excluding portions of the SFDs with resolution roll off from the camera resolution). The NB curve is similar to the 4%-5% SFD exponential model curves and shares a common number of fragmentation events and probability of failure as the Spirit and Phoenix SFD of rocks. This commonality in fragmentation to produce landing sites dominated by fine particles with low rock abundance suggests that the global, meters-thick surface layer on Mars, made up mostly of find-grained materials, can be produced mainly by impact cratering during the Amazonian.

Data Availability Statement

All InSight image data are available in the NASA Planetary Data System Geosciences node (https://pds-geosciences.wustl.edu/missions/insight/index.htm). All other Mars imaging data, including HiRISE images, are available in the NASA Planetary Data System Cartography and Imaging Node (https://pds-imaging.jpl.nasa.gov/). The HiRISE orthoimage and DEM in which the lander is located (Figure 18) are available at the University of Arizona, Lunar and Planetary Laboratory HiRISE image catalog at https://www.uahirise.org/dtm/dtm.php?ID=ESP_037262_1845 (Fergason et al., 2017), (along with other HiRISE images at https://hirise.lpl.arizona.edu/) and the orthoimage used to prepare Figure 18 is also available in the California Institute of Technology Research Data Repository in Golombek (2020). The non-map projected HiRISE image ESP_036761_1845 used to prepare Figure 7 is available at the University of Arizona, Lunar and Planetary Laboratory HiRISE image catalog at https://www.uahirise.org/ESP_036761_1845. The morning, midday (afternoon), and evening InSight IDC panoramas used to create Figures 8–15 are also available in the California Institute of Technology Research Data Repository in Golombek (2020). The IDC orthomosaic, DEM, and shape files of rocks measured in the near field (Figure 1) are available in the California Institute of Technology Research Data Repository in Golombek (2021).

Acknowledgements
A portion of this work was supported by the InSight Project at the Jet Propulsion Laboratory, California Institute of Technology under a contract with the National Aeronautics and Space Administration. We thank Alfred McEwen for information and discussion about the HiRISE camera. This paper is InSight Contribution Number ICN-204.

References

Abarca, H., Deen, R., Hollins, G., Zamani, P., Maki, J., Tinio, A., et al. (2019). Image and data processing for InSight lander operations and science. *Space Science Reviews*, *215*(2), 22. https://doi.org/10.1007/s11214-019-0587-9

Arvidson, R., Adams, D., Bonfiglio, G., Christensen, P., Cull, S., Golombek, M., et al. (2008). Mars Exploration Program 2007 Phoenix landing site selection and characteristics. *Journal of Geophysical Research*, *113*, E00A03. https://doi.org/10.1029/2007JE003021

Binder, A. B., Arvidson, R. E., Guinness, E. A., Jones, K. L., Morris, E. C., Mutch, T. A., et al. (1977). The geology of the Viking Lander 1 site. *Journal of Geophysical Research*, *82*, 4439–51. https://doi.org/10.1029/js082i028p04439

Brown, W. K. (1989). A theory of sequential fragmentation and its astronomical applications. *J. Astrophys. Astr.*, *10*, 89–112. https://doi.org/10.1007/BF02714980

Brown, W. K., & Wohletz, K. H. (1995). Derivation of the Weibull distribution based on physical principles and its connection to the Rosin-Rammler and lognormal distributions. *Journal of Applied Physics*, *78*, 2758–2763. https://doi.org/10.1063/1.360073

Charalambous, C. (2014). *On the evolution of particle fragmentation with applications to planetary surfaces*. Imperial College London. PhD Thesis.

Charalambous, C., Golombek, M., Pike, T., Warner, N. H., Weitz, C., Ansan, V., et al. (2019). *Rock distributions at the InSight landing site and implications based on fragmentation theory*. Abstract #2812. Lunar and Planetary Institute.50th Lunar and Planetary ScienceHouston

Charalambous, C., McClean, J. B., Baker, M., Pike, W. T., Golombek, M., Lemmon, M., et al. (2020). Aeolian Vortex-dominated aeolian activity at InSight's landing site, Part 1: Multi-instrument observations, analysis and implications. *Journal of Geophysical Research, Planets*, *126*, e2020JE006757. https://doi.org/10.1029/2020JE006757

Christensen, P. R. (1986). The spatial distribution of rocks on Mars. *Icarus*, *68*(2), 217–238. https://doi.org/10.1016/0019-1035(86)90020-5

Christensen, P. R., & Moore, H. J. (1992). The Martian surface layer. In H. H. Kieffer, B. M. Jakosky, C. W. Snyder, & M. S. Matthews (Eds.), *Mars* (pp. 686–727). University of Arizona Press.

Craddock, R.A., & Golombek, M. P. (2016). Characteristics of terrestrial basaltic rock populations: Implications for Mars lander and rover science and safety. *Icarus*, *274*, 50–72. https://doi.org/10.1016/j.icarus.2016.02.042

Fergason, R., Kirk, R. L., Cushing, G., Galuzska, D. M., Golombek, M. P., Hare, T. M., et al. (2017). Analysis of local slopes at the InSight landing site on Mars. *Space Science Reviews*, *211*(1-4), 109–133. https://doi.org/10.1007/s11214-016-0292-x

Garvin, J. B., Mouginis-Mark, P. J., & Head, J. W. (1981). Characterization of rock populations on planetary surfaces: Techniques and a preliminary analysis of Mars and Venus. *Moon and Planets*, *24*, 355–387. https://doi.org/10.1007/bf00897109

Gilvarry, J. J. (1961). Fracture of brittle solids I. Distribution function for fragment size in single fracture (theoretical). *Journal of Applied Physics*, *32*, 391–399. https://doi.org/10.1063/1.1736016

Gilvarry, J. J., & Bergstrom, B. H. (1961). Fracture of brittle solids II. Distribution function for fragment size in single fracture (experimental). *Journal of Applied Physics*, *32*, 400–410. https://doi.org/10.1063/1.1736017

Golombek, M. (2020). *Data for "Assessment of InSight landing site predictions"* [data set from Golombek, Kass et al., 2020]. California Institute of Technology Research Data Repository (CaltechDATA). https://doi.org/10.22002/D1.1422

Golombek, M. (2021). Data for Golombek, Trussel et al. paper "InSight Rock size-frequency distributions on Mars" [Data set], Earth and Space Science. California Institute of Technology Research Data Repository (CaltechDATA). https://doi.org/10.22002/D1.2077

Golombek, M., Charalambous, C., Pike, W. T., & Sullivan, R. (2020). The origin of sand and dust on Mars: Evidence from the InSight landing site. 51st Lunar and Planetary Science. Abstract #2744. Lunar and Planetary Institute.

Golombek, M., Grant, J., Kipp, D., Vasavada, A., Kirk, R., Fergason, R., et al. (2012). Selection of the Mars Science Laboratory landing site. *Space Science Reviews*, *170*(1-4), 641–737. https://doi.org/10.1007/s11214-012-9916-y

Golombek, M., Huertas, A., Kipp, D., & Calef, F. (2012). Detection and characterization of rocks and rock size-frequency distributions at the final four Mars Science Laboratory landing sites. *International Journal of Mars Science and Exploration*, *7*, 1–22. https://doi.org/10.1555/mars.2012.0001

Golombek, M., Kass, D., Williams, N., Warner, N., Daubar, I., Piqueux, S., et al. (2020). Assessment of InSight landing site predictions. *Journal of Geophysical Research, Planets*, *125*, e2020JE006502. https://doi.org/10.1029/2020JE006502

Golombek, M., Kipp, D., Warner, N., Daubar, I. J., Fergason, R., Kirk, R. L., et al. (2017). Selection of the InSight landing site. *Space Science Reviews*, *211*(1-4), 5–95. https://doi.org/10.1007/s11214-016-0321-9

Golombek, M., & Rapp, D. (1997). Size-frequency distributions of rocks on Mars and Earth analog sites: Implications for future landed missions. *Journal of Geophysical Research*, *102*, 4117–4129. https://doi.org/10.1029/96JE03319

Golombek, M., Warner, N. H., Grant, J. A., Hauber, E., Ansan, V., Weitz, C. M., et al. (2020). Geology of the InSight landing site on Mars. *Nature Communications*, *11*, 1014. https://doi.org/10.1038/s41467-020-14679-1

Golombek, M., Williams, N., Warner, N. H., Parker, T., Williams, M. G., Daubar, I., et al. (2020). Location and setting of the Mars InSight lander, instruments, and landing site. *Earth and Space Science*, *7*, e2020EA001248. https://doi.org/10.1029/2020EA001248

Golombek, M. P., Charalambous, C., Pike, W. T., & Sullivan, R. (2018). *The origin of sand on Mars. 49th Lunar and Planetary Science*. Abstract #2319. Lunar and Planetary Institute.

Golombek, M. P., Cook, R. A., Moore, H. J., & Parker, T. J. (1997). Selection of the Mars Pathfinder landing site. *Journal of Geophysical Research*, *102*(E2), 3967–3988. https://doi.org/10.1029/96JE03318

Golombek, M. P., Crumpler, L. S., Grant, J. A., Greeley, R., Cabrol, N. A., Parker, T. J., et al. (2006). Geology of the Gusev cratered plains from the Spirit rover traverse. *Journal of Geophysical Research*, *111*, E02S07. https://doi.org/10.1029/2005JE002503

Golombek, M. P., Haldemann, A. F. C., Forsberg-Taylor, N. K., DiMaggio, E. N., Schroeder, R. D., Jakosky, B. M., et al. (2003). Rock size-frequency distributions on Mars and implications for Mars Exploration Rover landing safety and operations. *Journal of Geophysical Research*, *108*(E12), 8086. https://doi.org/10.1029/2002JE002035

Golombek, M. P., Huertas, A., Marlow, J., McGrane, B., Klein, C., Martinez, M., et al. (2008). Size-frequency distributions of rocks on the northern plains of Mars with special reference to Phoenix landing surfaces. *Journal of Geophysical Research*, *113*, E00A09. https://doi.org/10.1029/2007je003065

Golombek, M. P., Grant, J. A., Parker, T. J., Kass, D. M., Crisp, J. A., Squyres, S. W., et al. (2003). Selection of the Mars Exploration Rover landing sites. *Journal of Geophysical Research*, *108*(E12), 8072. https://doi.org/10.1029/2003JE002074

Golombek, M. P., Otero, R. E., Heverly, M. C., Ono, M., Williford, K. H., Rothrock, B., et al. (2017). Characterization of Mars Rover 2020 prospective landing sites leading up to the second downselection. Abstract #2333. In *48th Lunar and Planetary Science*. Lunar and Planetary Institute.Houston

Grant, J. A., Warner, N. H., Weitz, C. M., Golombek, M. P., Wilson, S. A., Baker, M., et al. (2020). Degradation of Homestead hollow at the InSight landing site based on the distribution and properties of local deposits. *Journal of Geophysical Research: Planets*, *125*, e2019JE006350. https://doi.org/10.1029/2019JE006350

Grant, J. A., Wilson, S. A., Ruff, S. W., Golombek, M. P., & Koestler, D. L. (2006). Distribution of rocks on the Gusev Plains and on Husband Hill, Mars. *Geophysical Research Letters*, *33*, L16202. https://doi.org/10.1029/2006GL026964

Hartmann, W. K. (1969). Terrestrial, lunar, and interplanetary rock fragmentation. *Icarus*, *10*, 201–213. https://doi.org/10.1016/0019-1035(69)90022-0

Hébrard, E., Listowski, C., Coll, P., Marticorena, B., Bergametti, G., Määttänen, A., et al. (2012). An aerodynamic roughness length map derived from extended Martian rock abundance data. *Journal of Geophysical Research*, *117*, E04008. https://doi.org/10.1029/2011JE003942

Heet, T. L., Arvidson, R. E., Cull, S. C., Mellon, M. T., & Seelos, K. D. (2009). Geomorphic and geologic settings of the Phoenix Lander mission landing site. *Journal of Geophysical Research*, *114*, E00E04. https://doi.org/10.1029/2009JE003416

Maki, J. N., Golombek, M., Deen, R., Abarca, H., Sorice, C., Goodsall, T., et al. (2018). The color cameras on the InSight lander. *Space Science Reviews*, *214*(105). https://doi.org/10.1007/s11214-018-0536-z

Mastropietro, M., Pajola, M., Cremonese, G., Munaretto, G., & Lucchetti, A. (2020). Boulder analysis on the Oxia Planum ExoMars 2022 Rover landing site: Scientific and engineering perspectives. *Solar System Research*, *54*(#6), 504–519. https://doi.org/10.1134/S0038094620060040

Moore, H. J., & Keller, J. M. (1990). Surface-material maps of Viking landing sites on Mars. Reports of Planetary Geology and Geophysics Program – 1989. *NASA Tech. Memo.*, *4210*, 533–535.

Moore, H. J., & Keller, J. M. (1991). Surface-material maps of Viking landing sites on Mars. Reports of Planetary Geology and Geophysics Program – 1990. *NASA Tech. Memo.*, *4300*, 160–162.

Moore, H. J., Spitzer, C. R., Bradford, K. Z., Cates, P. M., Hutton, R. E., & Shorthill, R. W. (1979). Sample fields of the Viking landers. *Journal of Geophysical Research*, *84*, 8365–8377. https://doi.org/10.1029/jb084ib14p08365

Nowicki, S. A., & Christensen, P. R. (2007). Rock abundance on Mars from the Thermal Emission Spectrometer. *Journal of Geophysical Research*, *112*, E05007. https://doi.org/10.1029/2006JE002798

Pajola, M., Rossato, S., Baratti, E., Pozzobon, R., Quantin, C., Carter, J., & Thollot, P. (2017). Boulder abundances and size-frequency distributions on Oxia Planum-Mars: Scientific implications for the 2020 ESA ExoMars rover. *Icarus*, *296*, 73–90. https://doi.org/10.1016/j.icarus.2017.05.011

Rosin, P., & Rammler, E. (1933). The laws governing the fineness of powdered coal. *Journal Inst. Fuel*, *7*, 29–36.

Russell, P. S., Grant, J. A., Williams, K. K., Carter, L. M., Brent Garry, W., & Daubar, I. J. (2013). Ground penetrating radar geologic field studies of the ejecta of Barringer Meteorite Crater, Arizona, as a planetary analog. *Journal of Geophysical Research*, *118*, 1915–1933. https://doi.org/10.1002/jgre.20145

Schröder, S. E., Carsenty, U., Hauber, E., Schulzeck, F., Raymond, C. A., & Russell, C. T. (2021). The boulder population of asteroid 4 Vesta: Size-frequency distribution and survival time. *Earth and Space Science*, *8*, e2019EA000941. https://doi.org/10.1029/2019EA000941

Turcotte, D. L. (1997). *Fractals and Chaos in Geology and Geophysics* (2nd ed.). Cambridge University Press.

Ward, J. G., Arvidson, R. E., & Golombek, M. (2005). The size-frequency and areal distribution of rock clasts at the Spirit landing site, Gusev crater, Mars. *Geophysical Research Letters*, *32*, L11203. https://doi.org/10.1029/2005GL022705

Warner, N. H., Grant, J. A., Wilson, S., Golombek, M. P., DeMott, A., Charalambous, C., et al. (2020). An impact crater origin for the InSight landing site at Homestead hollow: Implications for near surface stratigraphy, surface processes, and erosion rates. *Journal of Geophysical Research: Planets*, *125*, e2019JE006333. https://doi.org/10.1029/2019JE006333

Wohletz, K. H., Sheridan, M. F., & Brown, W. K. (1989). Particle size distributions and the sequential fragmentation/transport theory applied to volcanic ash. *Journal of Geophysical Research*, *94*(15), 15,703–15,721. https://doi.org/10.1029/JB094iB11p15703

Yingst, R. A., Cropper, K., Gupta, S., Kah, L. C., Williams, R. M. E., Blank, J., et al. (2016). Characteristics of pebble and cobble-sized clasts along the Curiosity rover traverse from sol 100 to 750: Terrain types, potential sources, and transport mechanisms. *Icarus*, *280*(2016), 72–92. https://doi.org/10.1016/j.icarus.2016.03.001

Yingst, R. A., Crumpler, L., Farrand, W. H., Li, R., & de Souza, P. (2010). Constraints on the geologic history of 'Home Plate' materials provided by clast morphology and texture. *Journal of Geophysical Research*, *115*, E00F13. https://doi.org/10.1029/2010JE003668

Yingst, R. A., Haldemann, A. F. C., Biedermann, K. L., & Monhead, A. M. (2007). Quantitative morphology of rocks at the Mars Pathfinder landing site. *Journal of Geophysical Research*, *112*, E06002. https://doi.org/10.1029/2005JE002582

Yingst, R. A., Kah, L. C., Palucis, M., Williams, R. M. E., Garvin, J., Bridges, J. C., et al. (2013). Characteristics of pebble- and cobble-sized clasts along the Curiosity rover traverse from Bradbury Landing to Rocknest. *Journal of Geophysical Research Planets*, *118*, 2361–2380. https://doi.org/10.1002/2013JE004435